
Fractional Spike Differential Equations Neural Network with Efficient Adjoint Parameters Training

Chengjie Ge^{1,*}, Yufeng Peng^{1,*}, Xueyang Fu¹, Qiyu Kang^{1†},
Xuhao Li², Qixin Zhang³, Junhao Ren³, Zheng-Jun Zha¹

¹University of Science and Technology of China,

²Anhui University,

³Nanyang Technological University

Abstract

Spiking Neural Networks (SNNs) draw inspiration from biological neurons to create realistic models for brain-like computation, demonstrating effectiveness in processing temporal information with energy efficiency and biological realism. Most existing SNNs assume a single time constant for neuronal membrane voltage dynamics, modeled by first-order ordinary differential equations (ODEs) with Markovian characteristics. Consequently, the voltage state at any time depends solely on its immediate past value, potentially limiting network expressiveness. Real neurons, however, exhibit complex dynamics influenced by long-term correlations and fractal dendritic structures, suggesting non-Markovian behavior. Motivated by this, we propose the Fractional SPIKE Differential Equation neural network (fspikeDE), which captures long-term dependencies in membrane voltage and spike trains through fractional-order dynamics. These fractional dynamics enable more expressive temporal patterns beyond the capability of integer-order models. For efficient training of fspikeDE, we introduce a gradient descent algorithm that optimizes parameters by solving an augmented fractional-order ODE (FDE) backward in time using adjoint sensitivity methods. Extensive experiments on diverse image and graph datasets demonstrate that fspikeDE consistently outperforms traditional SNNs, achieving superior accuracy, comparable energy efficiency, reduced training memory usage, and enhanced robustness against noise. Our approach provides a novel open-sourced computational toolbox for fractional-order SNNs, widely applicable to various real-world tasks. Our source code can be found at: fspikeDE.

1 Introduction

Neural networks have undergone substantial evolution in recent decades as researchers continuously explore models that more accurately capture the complexities of biological neural systems while maintaining strong performance. Traditional artificial neural networks (ANNs) have achieved remarkable success in various machine learning tasks [1–6]. However, they operate fundamentally differently from the mechanisms observed in biological neural systems, and the computational power required to run modern deep learning models far exceeds that of human brains [7]. This disparity has motivated the development of Spiking Neural Networks (SNNs) [8–15], which attempt to model neural activity more realistically by communicating through discrete spikes rather than continuous values. SNNs have demonstrated considerable potential for processing temporal information with high energy efficiency [16–22]. Their event-driven computation paradigm allows for significant energy savings, particularly when implemented on neuromorphic hardware. Additionally, SNNs

*Equal contribution.

†Correspondence to: Qiyu Kang <qiyukang@ustc.edu.cn>.

incorporate a temporal dimension inherently into their processing, making them naturally suited for tasks involving time-series data or real-time interactions with dynamic environments [23–27]. These properties position SNNs as promising candidates for applications where energy efficiency and temporal processing are critical considerations.

Despite these advantages, most existing SNN models rely on first-order ordinary differential equations (ODEs) to describe neuronal membrane voltage dynamics [28–31]. These include the most commonly used Integrate-and-Fire (IF) and Leaky Integrate-and-Fire (LIF) models.

These models assume a single time constant, leading to a Markovian property where the current state depends only on the immediate previous state. While this simplification enables computational tractability, it also fundamentally limits the expressiveness of these networks. Biological neurons exhibit far more complex dynamics that include long-term dependencies and memory effects that cannot be adequately captured by integer-order models [32–35]. Neurophysiological research has demonstrated that real neurons display behaviors influenced by long-term correlations [36], fractal dendritic structures [37, 38], and the interaction of multiple active membrane conductances [33, 34]. These characteristics suggest that non-Markovian dynamics play a significant role in biological neural computation. Models that incorporate these effects could potentially achieve greater computational capacity and biological realism. Fractional calculus offers mathematical tools for modeling systems that exhibit memory effects and long-range dependencies [39, 40]. In contrast to integer-order calculus, fractional derivatives and integrals consider the entire history of a function, weighted by a power-law kernel. This inherent property makes fractional calculus particularly well-suited for describing systems with memory effects or non-local interactions—characteristics that align closely with the observed behaviors of biological neurons. The fractional leaky integrate-and-fire (Fractional-LIF) model, introduced and studied in [41, 42], serves as an example of applying these concepts. This model can effectively explain spiking frequency adaptations observed in pyramidal neurons [43] and has been shown to generate more reliable spike patterns than integer-order models when subjected to noisy input [41]. Despite these promising findings, the integration of SNNs and fractional calculus remains a relatively unexplored area.

In this paper, we introduce the Fractional SPIKE Differential Equation neural network (fspikeDE), a novel SNN network architecture that incorporates fractional-order dynamics into the modeling of neuronal membrane potentials. By replacing the first-order ODEs traditionally used in SNNs with fractional-order ODEs (FODEs), fspikeDE can capture long-term dependencies that are beyond the capability of standard SNN models, leading to improved performance on tasks that require complex temporal processing. Training neural networks with fractional equation dynamics presents significant challenges, particularly when dealing with the memory-intensive nature of FODEs [44], which may lead to unsatisfactory performance [44]. To address this issue, we develop an efficient training algorithm based on adjoint sensitivity methods. This algorithm optimizes network parameters by solving an augmented FODE backward in time, substantially reducing memory requirements. In contrast, most other SNN training platforms, such as SpikingJelly [45], adopt a recurrent formulation and apply the generalized backpropagation algorithm to the large unrolled computational graph, i.e., Backpropagation Through Time (BPTT) [30, 46]. Our fractional adjoint sensitivity training approach makes training fractional SNNs computationally feasible while consuming less training memory.

FODEs are known for their robustness to perturbations [47, 48]. Recent work [47] has shown that neural FODE models achieve tighter output perturbation bounds compared to their integer-order counterparts when subjected to input perturbations. An additional advantage of our proposed fspikeDE framework is its superior robustness under such perturbations. We evaluate fspikeDE on multiple benchmark datasets, covering both image classification and graph learning tasks. Experimental results show that fspikeDE consistently outperforms conventional SNNs across various evaluation metrics. Moreover, it exhibits enhanced robustness to noisy inputs. These findings underscore the practical advantages of integrating fractional-order dynamics into SNNs and point to the broader applicability of this approach in real-world scenarios.

Main contributions. Our objective in this paper is to formulate a generalized fractional-order SNN framework. Our key contributions are summarized as follows:

- We propose fspikeDE, a novel neural network architecture that integrates FODEs into SNNs to capture long-term dependencies with non-Markovian dynamics. This work provides the community with a novel open-sourced toolbox for fractional-order SNNs, widely applicable to various tasks.

- We develop an efficient training algorithm based on adjoint sensitivity methods, which significantly reduces memory requirements compared to conventional approaches.
- We conduct extensive experiments on multiple datasets, demonstrating that fspikeDE consistently outperforms traditional SNNs, achieving superior accuracy, comparable energy efficiency, reduced training memory usage, and enhanced robustness against noise.

Related Work. A comprehensive review of relevant studies is in Appendix S1.

2 Preliminaries

This section briefly reviews essential concepts. We first introduce fractional calculus, which generalizes derivatives to non-integer orders and effectively models systems with memory or non-local dependencies. We then outline conventional SNN approaches based on discrete-time simulations of integer-order dynamics, which serve as a reference for our later advancements.

2.1 Fractional Calculus

We first provide a concise introduction to fractional-order derivatives. We then formulate both integer- and fractional-order ODEs, using the common LIF and Fractional-LIF neuronal membrane potential models as illustrative examples.

2.1.1 Fractional Operators

When examining a function $y(t)$ with respect to (w.r.t.) time t , we traditionally define the first-order derivative as the instantaneous rate of change:

$$\frac{dy(t)}{dt} := \lim_{\Delta t \rightarrow 0} \frac{y(t + \Delta t) - y(t)}{\Delta t}. \quad (1)$$

The literature offers various definitions of fractional derivatives [49]. We primarily focus on the Caputo fractional derivative [39], which has the notable advantage of allowing initial conditions to be specified in the same manner as integer-order differential equations, making it particularly suitable for modeling dynamical systems. We consider the case where the fractional order $\alpha \in (0, 1]$.

Definition 1 (Caputo Fractional Derivative). *For a function $y(t)$ defined over an interval $[a, b]$, its Caputo fractional derivative of order $\alpha \in (0, 1]$ is given by [39]:*

$${}^C D_{a+}^{\alpha} y(t) := \frac{1}{\Gamma(1 - \alpha)} \int_a^t (t - \tau)^{-\alpha} y'(\tau) d\tau, \quad (2)$$

where $y'(\tau)$ denotes the first-order derivative of $y(\tau)$.

Remark 1. *It is important to note that the Caputo fractional derivative (2) seamlessly generalizes the first-order derivative (1). When the order α approaches 1, the Caputo derivative ${}^C D_{a+}^{\alpha}$ converges to the standard first-order derivative $\frac{d}{dt}$ [39][Theorem 7.1]. Examining (2) reveals that the fractional derivative incorporates the historical states of the function through the integral term when $\alpha \in (0, 1)$, highlighting its memory-dependent characteristics.*

2.1.2 Integer- and Fractional-order ODEs and Numerical Solutions

A first-order ODE can be formulated as:

$$\frac{dy(t)}{dt} = f(t, y(t)), \quad t \in [a, b]. \quad (3)$$

Similarly, a FODE involving the Caputo fractional derivative (as defined in (2)) is given by:

$${}^C D_{a+}^{\alpha} y(t) = f(t, y(t)), \quad t \in [a, b]. \quad (4)$$

For both types of equations, an initial condition $y(a) = y_0$ is specified. Complex functions $f(t, y(t))$ typically lack exact analytical solutions, requiring numerical approximation methods.

Euler Method for Integer-order ODEs: For the integer-order ODE in (3), the Euler method provides a straightforward numerical solution. Let $h > 0$ be a discretization parameter (step size), creating a

uniform grid over $[a, b]$ defined by $\{t_k = a + kh : k = 0, 1, \dots, N\}$, where $N = (b - a)/h$ is the number of timesteps. Let y_k denote the numerical approximation of $y(t_k)$. The Euler method is:

$$y_{k+1} = y_k + h f(t_k, y_k), \quad k = 0, 1, \dots, N - 1, \quad (5)$$

with the initial value y_0 provided by the initial condition.

ABM-Predictor for FODEs: For the fractional-order ODE (4), the Adams–Bashforth–Moulton (ABM) predictor method [50] can be used to solve it numerically. Using the same discretization as above with $t_k = a + kh$ for $k = 0, 1, \dots, N$, the ABM-predictor approximation is given by:

$$y_k = y_0 + \frac{1}{\Gamma(\alpha)} \sum_{j=0}^{k-1} \mu_{j,k} f(t_j, y_j), \quad (6)$$

where the weight coefficients $\mu_{j,k}$ are defined as $\mu_{j,k} = \frac{h^\alpha}{\alpha} [(k - j)^\alpha - (k - 1 - j)^\alpha]$. Here, y_k represents the numerical approximation for $y(t_k)$. This method explicitly accounts for the memory effect inherent in fractional-order systems by incorporating the weighted contributions of all previous function evaluations, reflecting the nonlocal nature of the Caputo fractional derivative. When $\alpha = 1$, (6) reduces to (5), which again shows the compatibility between (1) and (2).

2.2 LIF, Fractional-LIF and Traditional Integer-Order Spiking Neural Networks

SNNs process information using discrete events called spikes, inspired by biological neurons. The core computational unit in an SNN is the spiking neuron model. In this section, we focus on the LIF neuron and its fractional-order extension (Fractional-LIF). Other variants, such as the IF neuron and its fractional versions, are described in Appendix S2.

2.2.1 LIF and Fractional-LIF Neuron

LIF Neuron: The dynamics of the membrane voltage $U(t)$ of an LIF neuron can be described by the following first-order ODE [31]:

$$\tau \frac{dU(t)}{dt} = -U(t) + RI_{\text{in}}(t). \quad (7)$$

where τ is the membrane time constant, R is the membrane resistance, and I_{in} is the input of the current time step. When the membrane voltage $U(t)$ reaches a certain threshold θ , the neuron fires a spike, and the reset term subtracts the threshold θ from the membrane potential:

$$\text{if } U(t^-) \geq \theta, \text{ then } U(t) \leftarrow U(t) - \theta. \quad (8)$$

Fractional-LIF Neuron: The Fractional-LIF model extends the LIF dynamics by replacing the first-order derivative with a Caputo fractional derivative ${}^C D_{a+}^\alpha$ of order $\alpha \in (0, 1]$ [41]:

$$\tau_\alpha {}^C D_{a+}^\alpha U(t) = -U(t) + RI_{\text{in}}(t). \quad (9)$$

where τ_α is the membrane constant for Fractional-LIF. This introduces a memory effect, meaning the current membrane potential depends on the entire history of the neuron's voltage, as shown in (4) and (6). Spiking and reset mechanisms are defined the same way as in the classical LIF model.

2.2.2 Traditional Spiking Neural Networks Based on LIF Neuron

In an SNN, neurons communicate through discrete spikes. Traditional SNNs are based on the neuron dynamics described in (7). To make this time-varying solution compatible with sequence-based neural network models, an approximate solution to (7) is often found using numerical methods. In the simplest case, the forward Euler method (5) is employed and we get

$$U_{k+1} = U_k + \frac{h}{\tau} (-U_k + RI_{\text{in},k}) = (1 - \frac{h}{\tau}) U_k + \frac{h}{\tau} RI_{\text{in},k}. \quad (10)$$

For computational efficiency, we adopt several simplifications. Assume that time t is discretized into sequential steps where the step size $h = 1$. To further reduce the number of hyperparameters, assume membrane resistance $R = 1\Omega$ and define $\beta := (1 - \frac{1}{\tau})$. This leads to the following iterative update for the membrane potential U_k at discrete time step k :

$$U_{k+1} = \beta U_k + (1 - \beta) I_{\text{in},k}. \quad (11)$$

In practical SNN implementations, the term $(1 - \beta)$ is incorporated into learnable weights W that connect pre-synaptic neurons to post-synaptic neurons. The input current is then expressed as $I_{\text{in},k} = WX_k$, where X_k represents the input spike pattern at time t_k . Incorporating the spiking mechanism and reset dynamics, the complete discrete LIF update becomes [31]:

$$U_{k+1} = \underbrace{\beta U_k}_{\text{decay term}} + \underbrace{WX_k}_{\text{input contribution}} - \underbrace{S_{\text{out},k}\theta}_{\text{reset mechanism}}. \quad (12)$$

The output spike $S_{\text{out},k} \in \{0, 1\}$ is a binary value determined by comparing the membrane potential to the threshold θ . If the neuron fires $S_{\text{out},k} = 1$, the reset term subtracts the threshold from the membrane potential in the next step (as shown above). The spike generation is defined as:

$$S_{\text{out},k} = \begin{cases} 1, & \text{if } U_k > \theta \\ 0, & \text{otherwise.} \end{cases} \quad (13)$$

Learning in SNNs: Training SNNs poses unique challenges due to the discrete and non-differentiable nature of spike events. To address this, the widely used method is the surrogate gradient approach [30], which enables gradient-based training by approximating the non-differentiable spike function with a smooth surrogate during the backward pass. A common surrogate function is the threshold-shifted sigmoid, which approximates the Heaviside step function H used in spike generation:

$$H(U - \theta) \approx \sigma(U) = \frac{1}{1 + e^{\theta - U}}. \quad (14)$$

This differentiable approximation enables gradient flow through spiking neurons while preserving their discrete firing behavior.

3 Fractional Spike Differential Equations Neural Network

We propose replacing the first-order ODE governing membrane voltage dynamics in traditional SNNs with fractional dynamics. Our model, fspikeDE, can thus capture long-term dependencies, leading to improved performance. This section presents the fspikeDE framework along with its efficient adjoint-based training algorithm.

3.1 Framework

Traditional SNNs, as discussed in Section 2.2.2, model neuronal dynamics using discretized first-order ODEs, often leading to a recurrent formulation like that in (12). These recurrent SNNs are typically trained using BPTT on unrolled computational graphs [30, 46]. However, this discretized recurrent computation presents significant challenges. Specifically, BPTT incurs substantial

memory overhead and computational inefficiency, especially when many time steps are needed for accurate temporal modeling or stability. This high memory demand stems from BPTT requiring storage of all intermediate neuronal states and activations at each time step for gradient computation. Consequently, memory requirements scale with the number of time steps, often becoming a critical bottleneck for deeper networks or longer sequences. Furthermore, fixed-interval (h) state updates are often ill-suited for irregular, event-based inputs. Real-world stimuli, particularly from event-based sensors, consist of sparse, asynchronous spike trains where precise timing is crucial. A uniform time grid can oversample quiet periods, wasting computation, or undersample active bursts, risking detail loss if h is too coarse. In contrast, event-driven simulation, which updates neurons only upon spike arrival, naturally aligns computation with the data’s temporal structure, improving both efficiency and temporal fidelity.

In contrast to these traditional approaches, our fspikeDE framework directly employs a fractional-order ODE system to define the membrane potential dynamics. The introduction of fractional calculus

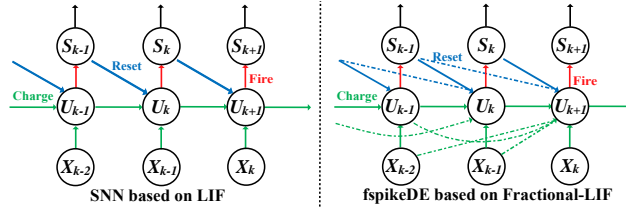


Figure 1: Comparison of traditional SNN and fspikeDE

aims to provide a more nuanced description of neuronal memory and adaptation. The core equation governing the membrane potential $U(t)$ of fspikeDE neurons is given by:

$$\tau_\alpha {}^C D_{a+}^\alpha U(t) = -U(t) + WX(t) - S_{\text{out}}(t)\theta. \quad (15)$$

Here, ${}^C D_{a+}^\alpha U(t)$ represents the Caputo fractional derivative of order α of the membrane potential $U(t)$ w.r.t. time t . The term $-U(t)$ describes the passive decay or leak of the membrane potential. $X(t)$ represents the input to the neuron, which is weighted by W . $S_{\text{out}}(t)$ is the output spike train of the neuron, and θ typically represents the spiking threshold. The output spike train is defined as:

$$S_{\text{out}}(t) = H(U(t) - \theta), \quad (16)$$

where H is the Heaviside step function. During model training with gradient descent, we replace the Heaviside step function with a differentiable surrogate function, e.g. (14). Various surrogate function options are available in the fspikeDE toolbox and are detailed in the Appendix S2.

Remark 2. *This fspikeDE framework offers considerable versatility: the weight matrix W can be implemented as either a dense matrix (forming a fully connected layer) or as a convolutional kernel (enabling the construction of convolutional layers). The right-hand side of (15) is presented as a LIF formulation, but other formulations such as IF are also available (see the Appendix S2). For numerical solutions to the FODE presented above, the ABM-predictor method described in (6) can be effectively employed. A comparison of information flow in fspikeDE and traditional SNNs is shown in Fig. 1, highlighting that fspikeDE incorporates historical states, thereby capturing long-term dependencies. The adjoint sensitive training of (15) is explained later in Section 3.3.*

The parameter α serves as a critical control mechanism for the memory effect within the system. When $\alpha = 1$, our model converges with traditional SNN formulations as discussed below. For values where $0 < \alpha < 1$, the model exhibits distinctive power-law memory characteristics, enabling more effective capture of long-term dependencies compared to conventional SNNs. Tasks requiring extensive historical information may benefit from smaller α values.

Relation To Traditional SNNs (12): When $\alpha = 1$, our model directly aligns with traditional SNN formulations. Specifically, setting $\alpha = 1$ and $\tau_\alpha = \tau$ transforms the fspikeDE equation into a first-order ODE $\tau \frac{dU(t)}{dt} = -U(t) + WX(t) - S_{\text{out}}(t)\theta$. When it is solved using Euler discretization (5) with step size $h = 1$ and defining $\beta := 1 - 1/\tau$, we obtain $U_{k+1} = \beta U_k + (1 - \beta)WX_k - (1 - \beta)S_{\text{out},k}\theta$. Through appropriate scaling of W and θ , this formulation reduces to the traditional SNN representation shown in (12). However, in the training stage, different from (12) that uses BPTT, we solve an adjoint backward ODE to compute the parameter gradient.

The fspikeDE framework is expected to be more robust than traditional SNNs. [41] showed that Fractional-LIF neuron modelling generates reliable spike patterns despite noisy input. Additionally, fractional-order models theoretically exhibit tighter output perturbation bounds against input perturbations than integer-order models [47]. Since fspikeDE is based on Fractional-LIF dynamics, it should benefit from this increased robustness to input noise. Our experiments in Section 4 confirm this, demonstrating fspikeDE’s superior performance under various noise levels.

3.2 Multi-Layer Formuation

The fspikeDE network may consist of multiple layers of Fractional-LIF neurons, with connections between neurons defined by learnable weight matrices. For a network of L layers, we let $U^{(l)}(t)$ and $X^{(l)}(t)$ denote the membrane potentials and inputs at layer l . Then we have

$$\tau_{\alpha,l} {}^C D_{a+}^\alpha U^{(l)}(t) = -U^{(l)}(t) + W^{(l)} X^{(l)}(t) - S_{\text{out}}^{(l)}(t)\theta^{(l)}, \text{ for each } l = 1, \dots, L. \quad (17)$$

with $X^{(1)}(t)$ the raw input and $X^{(l)}(t) = S_{\text{out}}^{(l-1)}(t)$ for $l > 1$. The membrane constant $\tau_{\alpha,l}$ can be specified for each layer l . The full network dynamics are governed by the coupled system (17), with each layer neuron’s membrane potential evolving according to its fractional dynamics and the input current determined by incoming spikes.

3.3 Adjoint-Based Training

To efficiently compute gradients w.r.t. network parameters, we adapt the adjoint sensitivity method for FODEs. This approach solves an augmented system of FODEs backward in time, significantly

reducing memory requirements compared to direct backpropagation through time. For classification problems, we predict the class based on the output neuron with the highest weighted firing rate (spike count). To track this metric, we introduce an augmented state $S_{\text{sum}}^{(L)}(t)$ with dynamics defined as:

$${}^C D_{a+}^\alpha S_{\text{sum}}^{(L)}(t) = S_{\text{out}}^{(L)}(t). \quad (18)$$

The cumulative spike count at time b is denoted as $S_{\text{sum}}^{(L)}(b)$. As a special case, when $\alpha = 1$ and the Euler method (5) is used, $S_{\text{sum}}^{(L)}(b) = h \sum_{k=0}^N S_{\text{out}}^{(L)}(t_k)$ represents the total spike count at the final layer. To train all parameters $\{W^{(l)}\}$, we minimize a loss function $\mathcal{L}(S_{\text{sum}}^{(L)}(b))$ using the fractional adjoint sensitivity method. By introducing the adjoint state $\lambda(t)$, we can have

$${}^C D_{b-}^\alpha \lambda(t) = - \left(\frac{\partial f}{\partial(U^{(1)}, \dots, U^{(L)}, S_{\text{out}}^{(L)})} \right)^\top \lambda(t), \quad \lambda(b) = \left(0, \dots, 0, \frac{\partial \mathcal{L}}{\partial S_{\text{sum}}^{(L)}(b)} \right). \quad (19)$$

Here, ${}^C D_{b-}^\alpha$ represents the right-Caputo fractional derivative, which is defined in Appendix S2, with numerical solutions following the same form as (6). The term f represents the concatenated dynamics from the right-hand side of (17), namely $f = \{-U^{(l)}(t) + W^{(l)} X^{(l)}(t) - S_{\text{out}}^{(l)}(t) \theta^{(l)}\}_{l=1}^L \cup \{S_{\text{out}}^{(L)}(t)\}$. The gradients w.r.t. parameters can then be computed as: $\frac{d\mathcal{L}}{dW} = \int_a^b \lambda(t)^\top \frac{\partial f}{\partial W} dt$. Further details on the derivation of the adjoint equation and model complexity analysis are in Appendix S3.

4 Experiments

In this section, we execute a series of SNN experiments over graph node classification and image classification tasks using our fspikeDE framework.

4.1 Graph Learning Tasks.

For graph learning tasks, our experiments focus on the following key aspects of evaluation: (1) **Node Classification** performance; (2) **Energy Efficiency**; and (3) the **Robustness** of the proposed fspikeDE model.

Dataset & Baselines. We conduct experiments on three mainstream GNN methods: SGCN [51], DRSGNN [52], and MSG [53], using several commonly used graph learning datasets. Specifically, Node Classification (NC) is performed with SGCN and DRSGNN on Cora [54], Citeseer [55], Pubmed [56], Photo, Computers, and ogbn-arxiv [57], while MSG-based models are evaluated on Computers, Photo, CS, and Physics [58]. To ensure fairness, we only replace the neuron modules in the baseline models with our proposed modules: Fractional-LIF Neuron for SGCN and DRSGNN, and Fractional-IF Neuron for MSG. We also include integer-order fspikeDE ($\alpha = 1$) as a reference baseline. Dataset details are provided in Appendix S4.

Experiment Setup. For node classification (NC) tasks based on SGCN and DRSGNN, we use Poisson encoding to generate spike data following a Poisson distribution. The number of timesteps N is set to 100, and the batch size is set to 32. The dataset is divided into training, validation, and test sets in the ratio of 0.7, 0.2 and 0.1. Additionally, for experiments based on DRSGNN, we set the dimension of the positional encoding to 32 and adopt the Laplacian eigenvectors (LSPE) [59] or random walk (RWPE) [60] method. All experiments are independently run 20 times, with the mean and standard deviation reported. The other experimental setting details are included in Appendix S4.

Table 1: Node Classification (NC) results in terms of classification accuracy (%) on multiple datasets. The best results are **boldfaced**, while the runner-ups are underlined. Standard deviations are provided as subscripts. I-fspikeDE denotes integer-order fspikeDE.

Methods	Cora	Citeseer	Pubmed	Photo	Computers	ogbn-arxiv
SGCN (SJ)	81.81 \pm 0.69	71.83 \pm 0.23	86.79 \pm 0.32	87.72 \pm 0.25	70.86 \pm 0.24	50.26 \pm 0.11
SGCN (I-fspikeDE)	<u>87.69\pm0.38</u>	<u>72.13\pm0.27</u>	<u>87.07\pm0.34</u>	92.49\pm0.32	<u>86.12\pm0.23</u>	51.10\pm0.14
SGCN (fspikeDE)	88.08\pm0.58	73.80\pm0.51	87.17\pm0.28	92.49\pm0.32	89.12\pm0.21	51.10\pm0.14
DRSGNN (SJ)	83.30 \pm 0.64	72.72 \pm 0.24	87.13 \pm 0.34	88.31 \pm 0.15	76.55 \pm 0.17	50.13 \pm 0.14
DRSGNN (I-fspikeDE)	<u>87.07\pm0.42</u>	<u>73.75\pm0.20</u>	<u>87.17\pm0.35</u>	91.93\pm0.20	<u>88.31\pm0.21</u>	53.13\pm0.13
DRSGNN (fspikeDE)	88.51\pm0.62	75.11\pm0.45	87.29\pm0.32	91.93\pm0.20	88.77\pm0.20	53.13\pm0.13

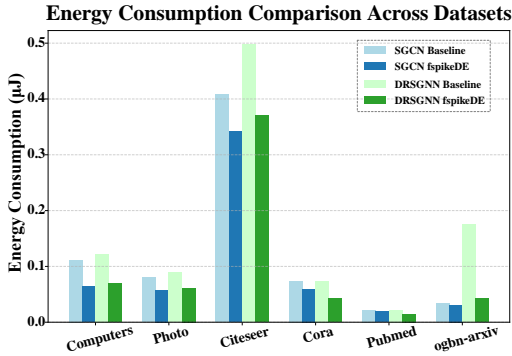
Node Classification Performance. The experimental results based on SGCN and DRSGNN are shown in Table 1. Our method outperforms the SGCN and DRSGNN methods implemented with SpikingJelly in terms of accuracy. Similarly, the experimental results based on MSG are shown in Table 2. Our method achieves significantly higher accuracy in node classification (NC) in the majority of cases compared to the MSG method implemented with SpikingJelly. These results highlight the clear advantage of our method in improving model accuracy.

Table 2: Node Classification (NC) results in terms of classification accuracy (%) on Multiple Datasets. The best results are **boldfaced**.

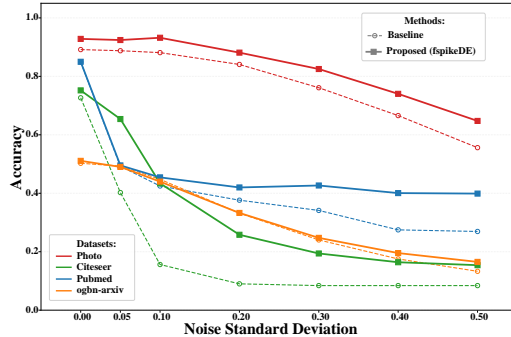
Methods	Computers	Photos	CS	Physics
MSG (SJ)	89.27 \pm 0.19	93.11 \pm 0.11	92.65 \pm 0.04	95.93\pm0.07
MSG (fspikeDE)	89.70\pm0.18	93.12\pm0.26	92.79\pm0.15	95.40 \pm 0.15

Table 3: Parameter Settings for Different Methods on Multiple Datasets.

Methods	Cora	Citeseer	Pubmed	Photo	Computers	ogbn-arxiv
SGCN (SJ)	7.680K	5.968K	22.224K	10.038K	1.503K	5.160K
SGCN (fspikeDE)	7.681K	5.969K	22.225K	10.039K	1.504K	5.161K
DRSGNN (SJ)	8.001K	5.968K	22.417K	10.038K	1.601K	6.441K
DRSGNN (fspikeDE)	8.002K	6.226K	22.418K	10.264K	1.601K	6.442K



(a) Comparison of energy consumption between SpikingJelly and fspikeDE.



(b) Robustness test for SGCN.

Figure 2: Energy consumption and robustness evaluation. Best zoomed on screen.

Energy Consumption Analysis. Following [9, 10], we compare the energy consumption of fspikeDE and SpikingJelly. Fig. 2a and Table 3 show that fspikeDE achieves higher accuracy and significantly lower energy consumption across datasets, even with comparable parameter counts, demonstrating its superior energy efficiency. Details will be discussed in the next section.

Robustness Test. We further validate the robustness advantage of fspikeDE. Specifically, we randomly add Gaussian noise [61] of varying intensities to the spike signals input to the network to evaluate the robustness of spiking graph neural networks under different noise conditions. The experimental results are shown in Fig. 2b. Details will be discussed in section 4.2.

4.2 Image Classification Tasks

For image classification tasks, our experiments focus on the following key evaluation aspects: (1) **Classification Performance**, (2) **Memory Usage and Energy Efficiency**, and (3) the **Robustness** of the proposed fspikeDE model.

Dataset & Baselines. We conduct comprehensive evaluations of the proposed fspikeDE model on static datasets MNIST [62] and Fashion-MNIST [63], as well as neuromorphic datasets DVS128Gesture [64] and N-Caltech101 [65]. The dataset details are provided in Appendix S4.

To ensure fairness and comparability, we adopt the same backbone network on the same datasets, differing only in the spiking neuron modules used. The baseline methods use the `neuron.LIFNode` module from SpikingJelly, while our method employs the Fractional-LIF Neuron module defined in fspikeDE. Additionally, we include integer-order fspikeDE ($\alpha = 1$) as a reference baseline in the comparative experiments to further validate the effectiveness of the proposed model.

Experimental Setup. We adopt a unified experimental setup for both the handwritten digit recognition dataset (MNIST) and the fashion image classification dataset (Fashion-MNIST). Specifically, the batch size is set to 512, and input spike signals are generated using `torch.bernoulli` to follow a Bernoulli distribution. The number of timesteps N is fixed at 16, and the models are trained for 100 epochs using the Adam optimizer. For neuromorphic datasets, we follow the preprocessing pipeline

provided by the SpikingJelly library, where event data is converted into frame-like representations with a unified setting of 16 timesteps. For the N-Caltech101 dataset, the datasets are split into training and test sets with a ratio of [0.8, 0.2] and resized to 128×128 before being fed into the network. The batch size for both neuromorphic datasets is set to 16, and the models are trained for 200 epochs using the Adam optimizer. All network architectures are based on CNN models. Detailed information about the network structures is provided in the Appendix S4.

Classification Performance. The experimental results on static and neuromorphic datasets are shown in Table 4 and 5. We compare the performance of the fspikeDE network with the baseline models. The results show that, under identical network configurations, fspikeDE consistently outperforms the baseline networks implemented with SpikingJelly.

Table 4: Image classifications results in terms of classification accuracy (%) on the MNIST and Fashion-MNIST datasets. The best results are **boldfaced**, while the runner-ups are underlined.

Methods	MNIST					Fashion-MNIST				
	Params	Train		Inference		Params	Train		Inference	
		Batch	Memory	Acc	Power		Batch	Memory	Acc	Power
Baseline	0.84M	512	14.3GB	<u>99.33</u>	0.038mJ	0.84M	512	14.3GB	90.92	0.039mJ
I-fspikeDE	0.84M	512	9.4GB	92.26	—	0.84M	512	9.4GB	<u>91.14</u>	—
fspikeDE	0.84M	512	6.2GB	99.39	0.015mJ	0.84M	512	7.9GB	91.27	0.018mJ

Table 5: Image classifications results in terms of classification accuracy (%) on the DVS128Gesture and N-Caltech101 datasets. The best results are **boldfaced**, while the runner-ups are underlined.

Methods	DVS128Gesture					N-Caltech101				
	Params	Train		Inference		Params	Train		Inference	
		Batch	Memory	Acc	Power		Batch	Memory	Acc	Power
Baseline	1.70M	16	16.2GB	<u>93.40</u>	5.38mJ	1.70M	16	16.2GB	66.82	8.81mJ
I-fspikeDE	1.70M	16	11.8GB	<u>93.40</u>	—	1.70M	16	11.8GB	<u>67.11</u>	—
fspikeDE	1.70M	16	9.5GB	95.87	3.89mJ	1.70M	16	9.5GB	70.26	7.96mJ

Memory Usage and Energy Efficiency. In terms of training memory usage, as shown in Table 4 and 5, fspikeDE significantly reduces memory consumption. For example, fspikeDE reduces training memory by 56.64% on the MNIST dataset and by 44.76% on the Fashion-MNIST dataset. On neuromorphic datasets like DVS128Gesture and N-Caltech101, fspikeDE achieves optimal performance while reducing training memory by 41.35%. Besides, we compare the energy consumption of fspikeDE and baseline networks during inference. As shown in Tables 4 and 5, fspikeDE significantly reduces training memory under the same network configurations while achieving higher energy efficiency. For instance, it reduces energy consumption by 60.53% on MNIST and 53.85% on Fashion-MNIST. Across all four datasets, fspikeDE consistently demonstrates lower energy consumption, validating its efficiency and practicality.

Robustness Analysis. We further validate the robustness advantage of fspikeDE. Specifically, we randomly add Gaussian noise to the spike signals input to the network to test the robustness of the network under different noise conditions. The experimental results are shown in Fig. 3. Compared to the baseline methods, fspikeDE demonstrates significantly stronger robustness under most noise conditions. Notably, under higher noise intensities, our method exhibits superior anti-interference capability. This advantage is primarily attributed to the Fractional-LIF Neuron module in fspikeDE, which is able to generate reliable patterns [41], thereby effectively enhancing the network’s noise suppression ability and improving the model’s robustness.

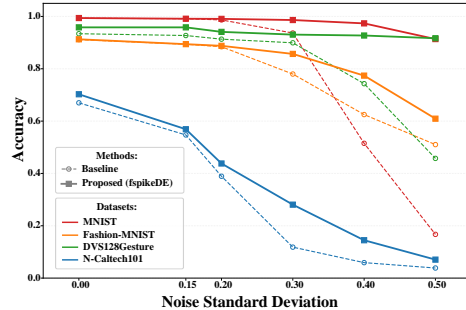


Figure 3: Robustness test on Image datasets.

The experimental results are shown in Fig. 3. Compared to the baseline methods, fspikeDE demonstrates significantly stronger robustness under most noise conditions. Notably, under higher noise intensities, our method exhibits superior anti-interference capability. This advantage is primarily attributed to the Fractional-LIF Neuron module in fspikeDE, which is able to generate reliable patterns [41], thereby effectively enhancing the network’s noise suppression ability and improving the model’s robustness.

5 Conclusion

In this paper, we introduced fspikeDE, a novel SNN framework that integrates fractional-order ODEs to effectively model long-term dependencies in neural processing. We developed an efficient training algorithm using adjoint sensitivity methods, which significantly reduces memory requirements compared to conventional backpropagation through time. Our extensive experiments on diverse image and graph datasets demonstrate that fspikeDE consistently outperforms traditional SNNs, achieving superior accuracy, enhanced robustness against noise, and reduced training memory usage, while maintaining comparable energy efficiency. The proposed fspikeDE and its accompanying open-sourced toolbox offer a promising direction for developing more expressive and biologically plausible SNNs for a wide range of real-world applications.

Appendix

This appendix complements the main body of our paper, providing additional details and supporting evidence for the assertions made therein. The structure of this document is as follows:

1. We discuss related work in appendix S1.
2. We offer more technical details about fractional calculus, spiking neurons, surrogate functions, and framework visualization in appendix S2.
3. We include theoretical results and complexity analysis in appendix S3
4. We present dataset statistics, experimental settings, and additional experimental results in appendix S4.
5. We show more details and usage of our fractional-order SNN toolbox, fspikeDE, in appendix S5.
6. We discuss the limitations of our work and its broader impact in the final section of this supplementary material.

S1 Related Work

S1.1 Spiking Neural Networks

Spiking Neural Networks (SNNs) have emerged as an important research area at the intersection of neuroscience and machine learning. Unlike traditional artificial neural networks (ANNs), SNNs process information through discrete spikes, similar to biological neurons. The foundational work on SNNs can be traced back to Hodgkin and Huxley’s biophysical model of neuronal dynamics [29], which provided a detailed description of action potential generation in neurons. While this model captured the biological mechanisms accurately, its computational complexity led to the development of simplified models more suitable for large-scale simulations. The Leaky Integrate-and-Fire (LIF) model [66] has become one of the most widely used neuron models in SNNs due to its balance between biological plausibility and computational efficiency. The LIF model describes the membrane potential dynamics using a first-order ordinary differential equation (ODE) with a leak term, and generates a spike when the potential exceeds a threshold. Various extensions to the LIF model have been proposed, including the Adaptive Exponential Integrate-and-Fire model [67], which incorporates adaptation mechanisms to better capture neuronal firing patterns. Recent years have seen significant advances in SNN architectures and applications. [68] provided a comprehensive review of deep learning approaches in SNNs, highlighting architectures that combine convolutional layers with spiking neurons. [16] explored the implementation of SNNs on neuromorphic hardware for energy-efficient computing. These developments have positioned SNNs as promising candidates for applications requiring low power consumption, such as edge computing and autonomous systems. Despite these advances, most existing SNN models rely on first-order ODEs with Markovian properties, which limit their ability to capture complex temporal dependencies. In this paper, we instead introduce a novel SNN network architecture that incorporates fractional-order dynamics into the modeling of neuronal membrane potentials.

S1.2 Fractional Calculus and Its Application in Neural Networks

Fractional calculus offers mathematical tools for modeling systems that exhibit memory effects and long-range dependencies [39, 40]. In contrast to integer-order calculus, fractional derivatives and integrals consider the entire history of a function, weighted by a power-law kernel. This inherent property makes fractional calculus particularly well-suited for describing systems with memory effects or non-local interaction. For example, in viscoelastic materials, fractional differential equations (FDEs) faithfully reproduce hereditary stress–strain relationships and long-term creep behavior [69]. In engineering contexts such as signal processing and automatic control, fractional differintegrals offer greater flexibility and accuracy in modeling dynamics than their integer-order counterparts [70].

The integration of FDEs has significantly advanced neural network studies. The combination of FDEs with neural network frameworks has proven especially valuable in neuroscientific computing [71, 72]. These studies have emphasized computational implementation while investigating the

stability characteristics and bifurcation phenomena in interconnected network structures [73–75]. The fractional leaky integrate-and-fire (Fractional-LIF) model is introduced and studied in [41, 42]. This model can effectively explain spiking frequency adaptations observed in pyramidal neurons [43] and has been shown to generate more reliable spike patterns than integer-order models when subjected to noisy input [41]. Recent developments have also merged FDE theory with ANNs. The work by [76, 77] proposed graph neural networks based on FDEs. Despite these promising findings, comprehensive frameworks for building and training fractional-order SNNs remain underdeveloped, particularly for large-scale learning tasks. The recent work [78, 79] trains SNNs using Caputo derivative-based gradient calculation. Recently [44] produced an initial exploration of SNN based on fractional calculus in simple machine learning tasks, but this combination did not improve classification accuracy. We argue that this is not true and propose the new fspikeDE framework. We introduce a gradient descent algorithm that optimizes parameters by solving an augmented FDE backward in time using adjoint sensitivity methods. Extensive experiments on diverse image and graph datasets demonstrate that fspikeDE consistently outperforms traditional SNNs, achieving superior accuracy, comparable energy efficiency, reduced training memory usage, and enhanced robustness against noise.

S1.3 Training Methods for Differential Equation-Based Neural Networks

The training of neural networks based on differential equations presents unique challenges, particularly regarding computational efficiency and gradient computation. Traditional methods for training such networks often involve discretizing the differential equations and applying backpropagation through time, which can be memory-intensive and computationally expensive. Neural ODEs [80, 81] represented an advancement in this area. They proposed treating neural network layers as continuous transformations defined by ODEs, and developed an adjoint-based method for computing gradients. This approach substantially reduced memory requirements during training by avoiding the need to store intermediate activations. Building on this work, [82] developed Latent ODEs for irregularly-sampled time series, demonstrating the potential of differential equation-based models for handling temporal data with variable sampling rates. Similarly, [83] extended the neural ODE framework to stochastic differential equations, enabling the modeling of systems with inherent randomness. For fractional differential equations specifically, the training challenges are even more pronounced due to the non-local nature of fractional derivatives. [84] proposes a scalable adjoint backpropagation method for training neural FDEs by solving an augmented FDE backward in time, which substantially reduces memory requirements. Several researchers have explored methods for training SNNs effectively [85]. Despite these advances, the adaptation of efficient training methods for fractional-order SNNs remains an open research area. The integration of adjoint-based methods with surrogate gradient techniques for training fractional SNNs represents a promising direction that has not been fully explored in the existing literature. Our work addresses this gap by developing a comprehensive framework for fractional-order SNNs, along with an efficient training algorithm based on adjoint sensitivity methods. This approach extends and combines ideas from neural ODEs, fractional calculus, and SNN training techniques to create a novel architecture with enhanced temporal processing capabilities.

S1.4 Event Camera

Event cameras, as novel bio-inspired sensors, capture pixel-level brightness changes through an asynchronous triggering mechanism [8]. With microsecond-level temporal resolution (equivalent to 10,000 fps) and a high dynamic range (140 dB) [86], they provide a groundbreaking solution for perception in high-speed dynamic scenes. Unlike traditional frame-based vision sensors, event cameras only record pixels undergoing changes in the scene, generating sparse event streams. This data structure not only significantly reduces redundant information but also enables robust perception under rapid motion and challenging lighting conditions. In the field of event stream processing, the asynchronous and sparse nature of event data poses challenges for conventional frame-based CNN algorithms. To address these challenges, researchers have proposed various encoding and processing methods tailored to the unique characteristics of event data. For instance, [87] introduced a surrogate gradient-based method to transform event streams into pulse sequences compatible with neural network processing. [88] proposed the Motion-Encoded Time-Surface (METS), which dynamically encodes pixel-level decay rates in time surfaces to capture the spatiotemporal dynamics reflected by events. This approach successfully addresses the challenge of pose tracking in high-speed scenarios using event cameras. Significant progress has also been made in network architecture optimization. [89] developed the STSC-SNN model, which introduces synaptic connections with

spatiotemporal dependencies, significantly enhancing the ability of spiking neural networks to process temporal information. Furthermore, event cameras, with their low latency and high dynamic range, have demonstrated broad application potential in fields such as robotic control, autonomous driving, and object tracking. For example, [90] proposed a 3D convolution-based spatiotemporal feature encoding method, utilizing a hierarchical separable convolution architecture to greatly improve the accuracy and efficiency of optical flow estimation in driving scenarios using event cameras. On the hardware optimization front, researchers have actively developed systems tailored for efficient event stream processing. [91] constructed a neuromorphic vision system based on the Intel Loihi 2 chip, achieving significantly lower power consumption compared to traditional GPU solutions, thus providing critical support for the efficient deployment of event cameras.

S2 More Technical Details

S2.1 More about Fractional Calculus

In Section 2.1 of the main paper, we presented the (left) Caputo fractional derivative and discussed numerical schemes for solving fractional-order ODEs. Here we provide additional background on fractional calculus that underpins our approach. For clarity, we note that throughout the main paper, all references to the Caputo fractional derivative specifically denote the left Caputo fractional derivative ${}^C D_{a+}^\alpha$. The sole exception appears in Section 3.3, where we employ the right Caputo fractional derivative ${}^C D_{b-}^\alpha$. Due to space constraints in the main text, we deferred the formal definition of the right Caputo derivative to this supplementary section, where we now provide a comprehensive treatment of both left and right fractional operators.

Classical Derivatives and Integrals

For a scalar function $y(t)$, the ordinary first-order derivative captures its instantaneous rate of change:

$$\frac{dy(t)}{dt} = \dot{y}(t) := \lim_{\Delta t \rightarrow 0} \frac{y(t + \Delta t) - y(t)}{\Delta t}. \quad (20)$$

Let J denote the integral operator that assigns to each function $y(t)$, which we assume to be Riemann integrable on the closed interval $[a, b]$, its antiderivative starting from a :

$$Jy(t) := \int_a^t y(\tau) d\tau \quad \text{for } t \in [a, b]. \quad (21)$$

When considering positive integers $n \in \mathbb{N}^+$, we write J^n to indicate the n -fold composition of J , where $J^1 = J$ and $J^n := J \circ J^{n-1}$ for $n \geq 2$. Through repeated integration by parts, one can show that [39][Lemma 1.1.]:

$$J^n y(t) = \frac{1}{(n-1)!} \int_a^t (t-\tau)^{n-1} y(\tau) d\tau \quad \text{for } n \in \mathbb{N}^+. \quad (22)$$

Extending to Non-Integer Orders: Fractional Integrals and Derivatives

Fractional Integrals Operators: Fractional integrals extend classical integration theory by allowing non-integer orders of integration. Among various formulations, the Riemann-Liouville fractional integrals are particularly fundamental [49][page 4]. For a positive real parameter $\alpha \in \mathbb{R}^+$, we define the left-sided and right-sided Riemann-Liouville fractional integral operators, denoted J_{left}^α and J_{right}^α , as follows:

$$\begin{aligned} J_{\text{left}}^\alpha y(t) &:= \frac{1}{\Gamma(\alpha)} \int_a^t (t-\tau)^{\alpha-1} y(\tau) d\tau, \\ J_{\text{right}}^\alpha y(t) &:= \frac{1}{\Gamma(\alpha)} \int_t^b (\tau-t)^{\alpha-1} y(\tau) d\tau, \end{aligned} \quad (23)$$

where $\Gamma(\alpha)$ represents the gamma function, which provides a continuous extension of the factorial operation to real and complex domains. The key distinction from classical repeated integration lies in the flexibility of the order parameter: while traditional calculus restricts the order n in (22) to positive

integers, the fractional order α in (23) spans the entire positive real line, enabling a continuous spectrum of integration orders.

Fractional Derivative Operators: Parallel to fractional integration, the concept of a fractional derivative extends the operation of differentiation to arbitrary non-integer orders. This allows for a more nuanced understanding of rates of change in complex systems.

One common formulation is the Riemann-Liouville fractional derivative. The left-sided (${}^{\text{RL}}D_{a+}^{\alpha}$) and right-sided (${}^{\text{RL}}D_{b-}^{\alpha}$) versions are formally defined by first applying a fractional integral and then an integer-order derivative [49]:

$$\begin{aligned} {}^{\text{RL}}D_{a+}^{\alpha}y(t) &:= \frac{d^m}{dt^m} J_{\text{left}}^{m-\alpha}y(t) = \frac{1}{\Gamma(m-\alpha)} \frac{d^m}{dt^m} \int_0^t \frac{y(\tau)d\tau}{(t-\tau)^{\alpha-m+1}} \\ {}^{\text{RL}}D_{b-}^{\alpha}y(t) &:= (-1)^m \frac{d^m}{dt^m} J_{\text{right}}^{m-\alpha}y(t) = \frac{(-1)^m}{\Gamma(m-\alpha)} \frac{d^m}{dt^m} \int_t^T \frac{y(\tau)d\tau}{(\tau-t)^{\alpha-m+1}}, \end{aligned} \quad (24)$$

Here, m is the smallest integer such that $m-1 < \alpha \leq m$.

Another widely used definition is the Caputo fractional derivative. The left-sided (${}^{\text{C}}D_{a+}^{\alpha}$) and right-sided (${}^{\text{C}}D_{b-}^{\alpha}$) Caputo derivatives are distinct from the Riemann-Liouville formulation in the order of operations: they involve first taking an integer-order derivative and then applying a fractional integral [49]. They are defined as follows:

$$\begin{aligned} {}^{\text{C}}D_{a+}^{\alpha}y(t) &:= J_{\text{left}}^{m-\alpha} \frac{d^m}{dt^m}y(t) = \frac{1}{\Gamma(m-\alpha)} \int_a^t \frac{\frac{d^m}{d\tau^m}y(\tau) d\tau}{(t-\tau)^{\alpha-m+1}}, \\ {}^{\text{C}}D_{b-}^{\alpha}y(t) &:= (-1)^m J_{\text{right}}^{m-\alpha} \frac{d^m}{dt^m}y(t) = \frac{(-1)^m}{\Gamma(m-\alpha)} \int_t^b \frac{\frac{d^m}{d\tau^m}y(\tau) d\tau}{(\tau-t)^{\alpha-m+1}}. \end{aligned} \quad (25)$$

The Caputo formulation offers several advantages: it produces zero when applied to constant functions (matching classical derivatives), and it accommodates standard initial conditions in differential equations, making it particularly suitable for modeling physical systems. We therefore choose the Caputo formulation.

A fundamental characteristic distinguishing fractional derivatives from their integer-order counterparts is their inherent non-locality. The integral representations in (24) and (25) reveal that fractional derivatives incorporate weighted contributions from the function's entire history on the interval $[a, t]$ (for left-sided) or $[t, b]$ (for right-sided). This memory effect contrasts sharply with classical derivatives, which depend only on infinitesimal neighborhoods around the evaluation point. The weighting kernel $(t-\tau)^{\alpha-m+1}$ determines how past states influence the present derivative value, with the fractional order α controlling the decay rate of this historical influence.

This memory-dependent nature makes fractional derivatives particularly valuable for modeling systems with hereditary properties, long-range interactions, or anomalous diffusion phenomena. In the limiting case where α approaches an integer value, these fractional operators smoothly transition to their classical counterparts [39], establishing fractional calculus as a genuine generalization of traditional calculus. For instance, when $\alpha = n \in \mathbb{N}$, both Riemann-Liouville and Caputo derivatives reduce to the standard n -th order derivative, ensuring theoretical consistency and practical applicability across the entire spectrum of differentiation orders. When dealing with vector-valued functions, the fractional operators act independently on each component, in direct analogy to the multivariate extension of ordinary differentiation and integration.

S2.2 More Variants of Neurons

In Section 2.2.1, we introduced the LIF and Fractional-LIF computational units. This section presents two additional variants: the IF and Fractional-IF neurons. Both fractional-order and first-order units (when $\alpha = 1$) are supported in our `fspikeDE` framework. Notably, `fspikeDE` also allows users to define custom neuron models by inheriting from the `BaseNeuron(nn.Module)` class provided in `neuron.py`.

IF Neuron: The membrane voltage dynamics $U(t)$ of an IF neuron are governed by the following first-order ODE:

$$\tau \frac{dU(t)}{dt} = RI_{\text{in}}(t). \quad (26)$$

where τ is the membrane time constant, R is the membrane resistance, and I_{in} is the input of the current time.

Fractional-IF Neuron: We define the Fractional-IF model, which extends the IF dynamics using fractional calculus:

$$\tau_\alpha {}^C D_{a+}^\alpha U(t) = R I_{\text{in}}(t). \quad (27)$$

where ${}^C D_{a+}^\alpha$ is the Caputo fractional derivative of order $\alpha \in (0, 1]$, and τ_α is the membrane constant for the Fractional-IF model. When $\alpha = 1$, the Fractional-IF model in (27) reduces to the standard IF model described by (26).

S2.3 Surrogate Functions in fspikeDE

Training SNNs presents a fundamental challenge: the spiking function (Heaviside step function) is non-differentiable, making standard backpropagation impossible. To address this, similar to other works [30], we employ surrogate gradient methods that replace the undefined derivative of the step function with smooth approximations during the backward pass. In the main paper, we present the threshold-shifted sigmoid function in (14). Our toolbox also implements other commonly used surrogate functions. We present them in this section.

For all surrogate functions, the forward pass computes the standard Heaviside step function:

$$H(x) = \begin{cases} 1, & \text{if } x \geq 0 \\ 0, & \text{if } x < 0 \end{cases} \quad (28)$$

The backward pass, however, replaces $H'(x)$ with a surrogate gradient $s(x)$. Below we detail each surrogate function implemented in our toolbox.

S2.3.1 Sigmoid Surrogate

The sigmoid surrogate uses the derivative of the scaled sigmoid function:

$$s_{\text{sigmoid}}(x) = \kappa \cdot \sigma(\kappa x) \cdot (1 - \sigma(\kappa x)) \quad (29)$$

where $\sigma(x) = \frac{1}{1+e^{-x}}$ is the sigmoid function and κ is a scaling parameter (default: $\kappa = 5.0$). This surrogate provides smooth gradients centered around the threshold, with the scale parameter controlling the sharpness of the approximation.

S2.3.2 Arctangent Surrogate

The arctangent surrogate employs the derivative of the arctangent function:

$$s_{\text{arctan}}(x) = \frac{\kappa}{1 + (\kappa x)^2} \quad (30)$$

where κ is the scale parameter (default: $\kappa = 2.0$). This function provides a bell-shaped gradient profile with heavier tails compared to the sigmoid surrogate, potentially allowing gradient flow for neurons further from the threshold.

S2.3.3 Piecewise Linear Surrogate

The piecewise linear surrogate defines a simple triangular approximation:

$$s_{\text{linear}}(x) = \begin{cases} \frac{1}{2\gamma}, & \text{if } -\gamma \leq x \leq \gamma \\ 0, & \text{otherwise} \end{cases} \quad (31)$$

where γ defines the width of the linear region (default: $\gamma = 1.0$). This surrogate provides constant gradients within a fixed window around the threshold, offering computational efficiency at the cost of gradient smoothness.

S2.3.4 Gaussian Surrogate

The Gaussian surrogate uses a normalized Gaussian function:

$$s_{\text{gaussian}}(x) = \frac{1}{\sigma\sqrt{2\pi}} \exp\left(-\frac{x^2}{2\sigma^2}\right) \quad (32)$$

where σ is the standard deviation parameter (default: $\sigma = 1.0$). This surrogate provides the smoothest gradient profile with exponential decay away from the threshold.

S2.3.5 Surrogate Gradient Implementation

In practice, during backpropagation through a spiking layer, the gradient of the loss \mathcal{L} with respect to the membrane potential u is computed as:

$$\frac{\partial \mathcal{L}}{\partial u} = \frac{\partial \mathcal{L}}{\partial s} \cdot s(u) \quad (33)$$

where s represents the spike output and $s(u)$ is the chosen surrogate gradient function. The choice of surrogate function and its hyperparameters impacts training dynamics, with sharper surrogates (larger scale parameters) providing more precise threshold behavior but potentially suffering from vanishing gradients.

S2.4 More about Framework and Its Visualization

In the main paper, we illustrate the distinct information flow characteristics of fspikeDE compared to traditional SNNs in Fig. 1. In conventional SNNs, the iterative nature of (12) results in skip connections. In contrast, fspikeDE utilizes dense connections, which arise from the weighted summation within the ABM predictor, as described in (6).

It is pertinent to clarify a subtle variation in some traditional SNN architectures. Often, the index in (12) is shifted by one, yielding:

$$U_{k+1} = \underbrace{\beta U_k}_{\text{decay term}} + \underbrace{W X_{k+1}}_{\text{input contribution}} - \underbrace{S_{\text{out},k}\theta}_{\text{reset mechanism}}. \quad (34)$$

This modification corresponds to the leftmost information flow diagram presented in Fig. 4. Essentially, this variant is equivalent to the middle diagram if the index of X_k is shifted. For a comprehensive overview, the full comparison of these information flows is provided in Fig. 4.

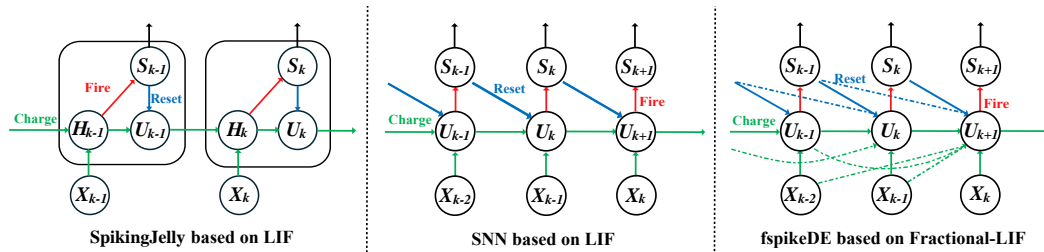


Figure 4: Comparison of traditional SNN and fspikeDE

S3 Theoretical Results and Complexity Analysis

S3.1 Discussion of Fractional-LIF Behavior

In this section, we compare the behavior between the LIF neuron and the Fractional-LIF neuron under a constant current input, which helps to understand the nuance of the fractional-order case. The results are not included in the main paper due to space limitations.

First, recall the equations from Section 2.2.1.

LIF Neuron: Recall the dynamics of the membrane voltage $U(t)$:

$$\tau \frac{dU(t)}{dt} = -U(t) + RI_{\text{in}}(t). \quad (35)$$

Fractional-LIF Neuron: Recall the dynamics of the membrane voltage $U(t)$:

$$\tau_\alpha {}^C D_{a+}^\alpha U(t) = -U(t) + RI_{\text{in}}(t). \quad (36)$$

Lemma 1. *Under a constant current input $I_{\text{in}}(t) \equiv I_{\text{const}}$, the solutions to the LIF dynamics (35) and the Fractional-LIF dynamics (36) are given by*

$$U(t) = RI_{\text{const}} + [U_0 - RI_{\text{const}}] e^{-\frac{t}{\tau}} \quad (37)$$

and

$$U(t) = RI_{\text{const}} + (U_0 - RI_{\text{const}}) E_\alpha \left(-\frac{t^\alpha}{\tau_\alpha} \right) \quad (38)$$

respectively, where U_0 is the initial initial membrane potential at $t = 0$ and $E_\alpha(z)$ is the Mittag-Leffler function defined as $E_\alpha(z) = \sum_{k=0}^{\infty} \frac{z^k}{\Gamma(\alpha k + 1)}$.

Remark 3. *Lemma 1 highlights the distinct ways membrane potential $U(t)$ relaxes towards the same steady-state value under constant current injection for standard LIF and Fractional-LIF neurons. In the LIF neuron, this relaxation is exponential. Conversely, the fractional-order model demonstrates altered relaxation dynamics due to its inherent memory effect, meaning the current membrane potential depends on the neuron's entire voltage history.*

Key properties include:

1. When $\alpha = 1$, the Mittag-Leffler function reduces to the exponential: $E_1(-t/\tau) = e^{-t/\tau}$, recovering the classical solution.
2. For $0 < \alpha < 1$, the Mittag-Leffler function exhibits:
 - Initial stretched exponential decay
 - Power-law tail for large t : $E_\alpha(-t^\alpha/\tau_\alpha) \sim \frac{\tau_\alpha}{\Gamma(1-\alpha)t^\alpha}$. These behaviors are visualized in Fig. 5.
3. The fractional model with $0 < \alpha < 1$ captures sub-diffusive relaxation processes, which can better represent certain biological membranes with anomalous diffusion or memory effects.

The additional degree of freedom introduced by $\alpha \in (0, 1]$ provides greater flexibility in modeling membrane voltage dynamics. This enhances the capacity of our fractional-order SNNs to encode long-term temporal dependencies, making them particularly suitable for tasks that require integration of extensive historical information. Notably, smaller α values tend to emphasize these long-range effects.

Proof. For the first-order case, we multiply both sides of (35) by $e^{t/\tau}$, yielding

$$e^{t/\tau} \frac{dU}{dt} + \frac{1}{\tau} e^{t/\tau} U = \frac{R}{\tau} I_{\text{const}} e^{t/\tau}.$$

This simplifies to

$$\frac{d}{dt} \left(U e^{t/\tau} \right) = \frac{R}{\tau} I_{\text{const}} e^{t/\tau}.$$

Integrating both sides with respect to t , we obtain

$$U(t) e^{t/\tau} = \int \frac{R}{\tau} I_{\text{const}} e^{t/\tau} dt + C = RI_{\text{const}} e^{t/\tau} + C,$$

where C is the constant of integration. Solving for $U(t)$, we find

$$U(t) = RI_{\text{const}} + C e^{-t/\tau}.$$

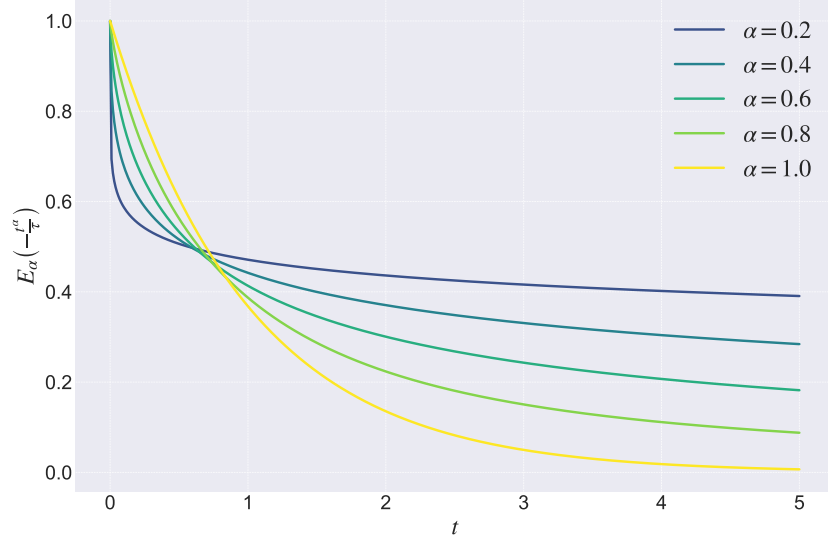


Figure 5: Visualization of Mittag-Leffler function $E_\alpha(-t^\alpha/\tau_\alpha)$. When $\alpha = 1$, it reduces to the exponential function $E_1(-t/\tau) = e^{-t/\tau}$.

Applying the initial condition $U(0) = U_0$, we get $U_0 = RI_{\text{const}} + C$. So $C = U_0 - RI_{\text{const}}$. Therefore, the solution is

$$U(t) = RI_{\text{const}} + (U_0 - RI_{\text{const}}) e^{-t/\tau}.$$

For the fractional case, we take a more general Laplace transform approach. Applying the Laplace transform to both sides of (36), and using the property

$$\mathcal{L}\{ {}^C D_t^\alpha U(t) \} = s^\alpha U(s) - s^{\alpha-1} U_0,$$

we obtain the transformed equation:

$$s^\alpha U(s) - s^{\alpha-1} U_0 + \frac{1}{\tau_\alpha} U(s) = \frac{RI_{\text{const}}}{\tau_\alpha} \cdot \frac{1}{s}.$$

Rearranging terms and solving for $U(s)$, we get:

$$U(s) \left(s^\alpha + \frac{1}{\tau_\alpha} \right) = s^{\alpha-1} U_0 + \frac{RI_{\text{const}}}{\tau_\alpha s}.$$

So we have

$$U(s) = \frac{s^{\alpha-1} U_0}{s^\alpha + \frac{1}{\tau_\alpha}} + \frac{RI_{\text{const}}}{\tau_\alpha} \cdot \frac{1}{s \left(s^\alpha + \frac{1}{\tau_\alpha} \right)}.$$

To simplify the second term, observe the partial fraction identity:

$$\frac{1}{s \left(s^\alpha + \frac{1}{\tau_\alpha} \right)} = \frac{\tau_\alpha}{s} - \frac{\tau_\alpha s^{\alpha-1}}{s^\alpha + \frac{1}{\tau_\alpha}}.$$

Substituting this expression, we obtain:

$$U(s) = \frac{s^{\alpha-1} U_0}{s^\alpha + \frac{1}{\tau_\alpha}} + RI_{\text{const}} \left(\frac{1}{s} - \frac{s^{\alpha-1}}{s^\alpha + \frac{1}{\tau_\alpha}} \right) = \frac{RI_{\text{const}}}{s} + \frac{s^{\alpha-1} (U_0 - RI_{\text{const}})}{s^\alpha + \frac{1}{\tau_\alpha}}.$$

Taking the inverse Laplace transform and using the identity

$$\mathcal{L}^{-1} \left\{ \frac{s^{\alpha-1}}{s^\alpha + a} \right\} = E_\alpha(-at^\alpha),$$

where $E_\alpha(\cdot)$ is the Mittag-Leffler function, we arrive at the time-domain solution:

$$U(t) = RI_{\text{const}} + (U_0 - RI_{\text{const}}) E_\alpha \left(-\frac{t^\alpha}{\tau_\alpha} \right).$$

□

S3.2 Adjoint Sensitivity Method

The fspikeDE network may consist of multiple layers of Fractional-LIF neurons, with connections between neurons defined by learnable weight matrices. For a network of L layers, we let $U^{(l)}(t)$ and $X^{(l)}(t)$ denote the membrane potentials and inputs at layer l . Note that $X^{(1)}(t)$ is the raw input and $X^{(l)}(t) = S_{\text{out}}^{(l-1)}(t)$ for $l > 1$. The membrane constant $\tau_{\alpha,l}$ can be specified for each layer l . The full network dynamics are governed by the following coupled system (39) and (40), with each layer neuron's membrane potential evolving according to its fractional dynamics and the input current determined by incoming spikes.

$$\begin{aligned} \tau_{\alpha,1} {}^C D_{a+}^\alpha U^{(1)}(t) &= -U^{(1)}(t) + W^{(1)} X^{(1)}(t) - S_{\text{out}}^{(1)}(t) \theta^{(1)}, \\ \tau_{\alpha,2} {}^C D_{a+}^\alpha U^{(2)}(t) &= -U^{(2)}(t) + W^{(2)} S_{\text{out}}^{(1)}(t) - S_{\text{out}}^{(2)}(t) \theta^{(2)}, \\ &\vdots \\ \tau_{\alpha,l} {}^C D_{a+}^\alpha U^{(l)}(t) &= -U^{(l)}(t) + W^{(l)} S_{\text{out}}^{(l-1)}(t) - S_{\text{out}}^{(l)}(t) \theta^{(l)}, \\ &\vdots \\ \tau_{\alpha,L} {}^C D_{a+}^\alpha U^{(L)}(t) &= -U^{(L)}(t) + W^{(L)} S_{\text{out}}^{(L-1)}(t) - S_{\text{out}}^{(L)}(t) \theta^{(L)}. \end{aligned} \quad (39)$$

To efficiently compute gradients w.r.t. network parameters, we adapt the adjoint sensitivity method for FODEs [84]. This approach solves an augmented system of FODEs backward in time, significantly reducing memory requirements compared to direct backpropagation through time. For classification problems, we predict the class based on the output neuron with the highest weighted firing rate (spike count). To track this metric, we introduce an augmented state $S_{\text{sum}}^{(L)}(t)$ with dynamics defined as:

$${}^C D_{a+}^\alpha S_{\text{sum}}^{(L)}(t) = S_{\text{out}}^{(L)}(t). \quad (40)$$

The cumulative spike count at time b is denoted as $S_{\text{sum}}^{(L)}(b)$. As a special case, when $\alpha = 1$ and the Euler method (5) is used, $S_{\text{sum}}^{(L)}(b) = h \sum_{k=0}^N S_{\text{out}}^{(L)}(t_k)$ represents the total spike count at the final layer, scaling by h . To train all parameters $\{W^{(l)}\}$, we minimize a loss function $\mathcal{L}(S_{\text{sum}}^{(L)}(b))$ using the fractional adjoint sensitivity method as follows.

By introducing the adjoint state $\lambda(t)$, we apply the fractional-order adjoint method proposed in [84] to derive the adjoint state dynamics for the coupled system described in (39) and (40). This approach utilizes the gradients of the surrogate functions introduced in appendix S2.3. The adjoint state evolves according to:

$${}^C D_{b-}^\alpha \lambda(t) = - \left(\frac{\partial f}{\partial (U^{(1)}, \dots, U^{(L)}, S_{\text{out}}^{(L)})} \right)^\top \lambda(t), \quad (41)$$

$$\text{with } \lambda(b) = \left(0, \dots, 0, \frac{\partial \mathcal{L}}{\partial S_{\text{sum}}^{(L)}(b)} \right). \quad (42)$$

Here, ${}^C D_{b-}^\alpha$ represents the right-Caputo fractional derivative, which is defined in (25). The term f represents the concatenated dynamics from the right-hand side of (39) and (40), expressed as:

$$f = \left\{ -U^{(l)}(t) + W^{(l)} X^{(l)}(t) - S_{\text{out}}^{(l)}(t) \theta^{(l)} \right\}_{l=1}^L \cup \left\{ S_{\text{out}}^{(L)}(t) \right\}. \quad (43)$$

The initial condition $\lambda(b)$ in (42) includes $\frac{\partial \mathcal{L}}{\partial S_{\text{sum}}^{(L)}(b)}$ while all other elements are set to 0. This setup indicates that, in our experiments, the loss depends solely on the final cumulative spike count at layer L . If the loss function is designed to depend on other states, such as $U^{(L)}(b)$, the corresponding elements in (42) should instead be updated to $\frac{\partial \mathcal{L}}{\partial U^{(L)}(b)}$. According to [84][Eq.16], the gradients w.r.t. parameters $W = \cup_l \{W^{(l)}\}$ can then be computed as:

$$\frac{d\mathcal{L}}{dW} = \int_a^b \lambda(t)^\top \frac{\partial f}{\partial W} dt. \quad (44)$$

To numerically solve (41) and (44), we apply the discretization methods introduced in (5) and (6).

S3.3 Complex Analysis

In the forward integration of (39) and (40) using the ABM predictor (6), at each time-step t_j we must evaluate the fractional derivative $f(t_j, y_j)$ and retain these values for later use. Here, f refers to the right-hand side defined in (43), and the hidden state is defined as

$$y_j := \left\{ U^{(l)}(t_j) \right\}_{l=1}^L \cup \left\{ S_{\text{out}}^{(L)}(t_j) \right\},$$

covering all L layers plus the final spike-count state. If there are $N = T/h$ steps in total, then summing the base cost C per evaluation with the growing cost $O(k)$ of accumulating k -term histories yields $\sum_{k=0}^N (C + O(k)) = O(NC + N^2)$. By leveraging a fast convolution routine (e.g. the FFT-based method of [92]), the quadratic term can be reduced to $O(N \log N)$, giving an overall forward-pass cost of $O(NC + N \log N)$. Since each step also stores its hidden state vector of dimension d , and computing f at one timestamp incurs a peak memory P , the forward memory requirement grows as

$$O(P + Nd)$$

where the Nd term accounts for saving all N evaluations $\{f(t_j, y_j)\}_{j=1}^N$.

When performing the backward (adjoint) computation as in (41) and (44), we must carry out a chain of vector-Jacobian products. Per the analysis in [93], this costs on the order of two to three times a single evaluation of f . Thus, the backward-pass time complexity again scales like $O(NC + N^2)$ or—in the FFT-accelerated variant— $O(NC + N \log N)$. If storing the adjoint-weight product $\lambda \partial f / \partial W$ requires memory Q , then the peak memory during backpropagation is

$$O(Q + Nd)$$

since $\lambda \partial f / \partial W$ has the same dimensionality as the state vector.

By contrast, naively differentiating through all forward-pass steps (i.e. unrolling (6) and retaining every intermediate state and its parameter gradients) would demand storing, at each of the N time steps, both the state and its full gradient of size Q . This leads to a storage burden

$$O(NQ + Nd)$$

which for large parameter matrices W (where Q typically exceeds d in modern network architecture like Transformer Attentions) can greatly exceed the $O(Q + Nd)$ memory profile of the adjoint method.

For comparison, traditional SNNs, as discussed in Section 2.2.2, model neuronal dynamics using discretized first-order ODEs, often leading to a recurrent formulation like that in (12). These recurrent SNNs are typically trained using BPTT on unrolled computational graphs [30, 46]. This discretized recurrent computation presents significant challenges. BPTT incurs substantial memory overhead and computational inefficiency, especially when many time steps are needed for accurate temporal modeling. The memory cost for BPTT requires $O(NQ + Nd)$ which is the same as the above naively differentiating, assuming N time steps.

Finally, note that one can trim the $O(Nd)$ storage of all past $f(t_j, y_j)$ values down to $O(Kd)$ by invoking the “short-memory” approximation—keeping only the most recent K terms in the fractional derivative sum as in [94, 95].

S4 Implementation Details and Dataset Specifics

S4.1 Experiment Settings

S4.1.1 Graph Learning Tasks.

Datasets & Baselines. Our experiments evaluate model performance on a diverse collection of graph-structured datasets spanning multiple domains, following standard preprocessing protocols in geometric deep learning, with their detailed statistics summarized in Table 6. Specifically, Node Classification (NC) is performed with SGCN and DRSGNN on Cora, Citeseer, Pubmed, Photo, Computers, and ogbn-arxiv. MSG-based models are evaluated on Computers, Photo, CS, and Physics. Additionally, we conduct Link Prediction (LP) experiments with MSG-based methods on the same datasets, with results presented in the following section.

Table 6: Dataset Statistics of Node Classification Task

Name	# of Nodes	# of Classes	# of Features	# of Edges
Cora	2,708	7	1,433	10,556
Pubmed	19,717	3	500	88,648
Citeseer	3,327	6	3,703	9,104
Photo	7,650	8	745	238,162
Computers	13,752	10	767	491,722
OGBN-Arxiv	169,343	40	128	1,166,243
CS	18,333	15	6,805	163,788
Physics	34,493	5	8,415	495,924

Training& Inference settings. For node classification (NC) tasks based on SGCN and DRSGNN, we use Poisson encoding to generate spike data following a Poisson distribution. The number of timesteps N is set to 100, and the batch size is set to 32. The dataset is divided into training, validation, and test sets in the ratio of 0.7, 0.2 and 0.1. Additionally, for experiments based on DRSGNN, we set the dimension of the positional encoding to 32 and adopt the Laplacian eigenvectors (LSPE) [59] or random walk (RWPE) [60] method. For NC and link Prediction (LP) tasks on MSG, we follow the experimental settings described in the original MSG paper. Specifically, we use IF neurons and the Lorentz model, set the dimension of the representation space to 32, and configure the timesteps to [5, 15]. The optimizer used is Adam, with an initial learning rate of 0.001. All experiments are independently run 20 times, with the mean and standard deviation reported.

S4.1.2 Image Classification Tasks.

Datasets & Baselines. We conducted experiments on four visual classification tasks, including the static handwritten dataset **MNIST**, the static fashion image dataset **Fashion-MNIST**, and two neuromorphic datasets, **DVS128Gesture** and **N-Caltech101**. **MNIST** is a classic dataset for handwritten digit recognition, comprising 10 classes of grayscale images (digits 0–9). It is widely used as a benchmark in fundamental research on image classification. The dataset contains 60,000 training samples and 10,000 test samples, with each image having a resolution of 28×28 pixels. **Fashion-MNIST** is an extended version of MNIST designed to provide a more challenging and application-oriented dataset. Similar to MNIST, Fashion-MNIST consists of 60,000 training samples and 10,000 test samples, with each image also having a resolution of 28×28 pixels. Each grayscale image represents a clothing category (e.g., T-shirt, trousers, shoes), with a total of 10 classes. Compared to MNIST, Fashion-MNIST exhibits more complex patterns with richer texture and shape variations. The classification task requires models to correctly predict the clothing category, which is more challenging and closer to real-world scenarios. **DVS128Gesture** is a neuromorphic dataset collected using a Dynamic Vision Sensor (DVS) event camera, designed for dynamic gesture recognition tasks. The event camera captures pixel-level brightness changes with microsecond temporal resolution. The dataset includes 1,342 samples across 11 gesture categories, such as clockwise rotation, counterclockwise rotation, and left-hand waving. **N-Caltech101** is an event camera-based dataset derived from the traditional static image dataset Caltech101. The original Caltech101 dataset contains 101 object categories (e.g., animals, vehicles, household items), with each category containing 40 to 800 static images. By simulating translational, rotational, and other movements, event cameras dynamically capture these

static images to generate the corresponding neuromorphic data. Similar to DVS128Gesture, the data from N-Caltech101 is represented as event streams, which encode pixel-wise brightness changes over time. The classification task focuses on recognizing object categories in dynamic scenes.

Training& Inference settings. We adopt a unified experimental setup for both the handwritten digit recognition dataset (MNIST) and the fashion image classification dataset (Fashion-MNIST). Specifically, the batch size is set to 512, and input spike signals are generated using `torch.bernoulli` to follow a Bernoulli distribution. The number of timesteps N is fixed at 16, and the models are trained for 100 epochs using the Adam optimizer. For neuromorphic datasets, we follow the preprocessing pipeline provided by the SpikingJelly library, where event data is converted into frame-like representations with a unified setting of 16 timesteps. For the N-Caltech101 dataset, the datasets are split into training and test sets with a ratio of [0.8, 0.2] and resized to 128×128 before being fed into the network. The batch size for both neuromorphic datasets is set to 16, and the models are trained for 200 epochs using the Adam optimizer.

All network architectures are based on CNN models. Detailed information about the network structures is provided in Table 8, Table 9, Table 10 and Table 11.

S4.2 Extended Experimental Results

S4.2.1 Link Prediction.

The experimental results for Link Prediction (LP) are presented in Table 2. Our method, MSG (fspikeDE), consistently outperforms MSG (SJ) across all datasets in terms of area under curve. Specifically, MSG (fspikeDE) achieves the best performance on the Computers, Photos, CS, and Physics datasets, with area under curve of 94.91%, 96.80%, 96.53%, and 96.57%, respectively.

Table 7: Link Prediction (LP) results in terms of Area Under Curve (AUC) (%) on multiple datasets. The best results are **boldfaced**.

Methods	Computers	Photos	CS	Physics
MSG (SJ)	94.65 \pm 0.73	96.75 \pm 0.18	95.19 \pm 0.15	93.43 \pm 0.16
MSG (fspikeDE)	94.91 \pm 0.12	96.80 \pm 0.16	96.53 \pm 0.15	96.57 \pm 0.08

Compared to the MSG method implemented with SpikingJelly, our fspikeDE approach provides significant improvements, demonstrating its effectiveness in enhancing link prediction tasks. These results highlight the significant performance improvements achieved by fspikeDE across diverse datasets, demonstrating its effectiveness in link prediction tasks.

S4.2.2 Extended Robustness Experiments.

To further verify the robustness advantages of fspikeDE, we designed and conducted a series of experiments for investigation.

Graph Learning Tasks.

Robustness to Feature Masking Ratios in Graph Learning. To evaluate the robustness of the network in graph learning tasks, we conducted feature ablation experiments on two benchmark datasets: Photo and Computers. Specifically, we implemented a random feature masking strategy where a proportion of features in the graph feature matrix were zeroed out according to predefined ratios. This is to test the irregular sampling scenarios with partially observed multivariate event series. The modified feature matrices were then fed into the models for prediction accuracy evaluation. As shown in Figure 6, our proposed fspikeDE method demonstrates significantly improved performance compared to the spikingjelly baseline method across all tested missing rates. This consistent superiority under varying feature dropout scenarios substantiates the enhanced robustness of our approach against input perturbations.

Structural Robustness Under Edge Dropout Scenarios. To comprehensively evaluate the robustness the network in graph-structured data learning, we conducted edge perturbation experiments on two classical citation network datasets: Cora and Citeseer . Specifically, we implemented a random edge masking strategy where a predefined proportion of edges in the graph adjacency matrix were randomly zeroed out according to controlled corruption ratios. The modified adjacency matrices were

then utilized for model evaluation through standard prediction accuracy metrics. As illustrated in Figure 7, our proposed fspikeDE framework demonstrates superior performance compared to the spikingjelly baseline across varying edge dropout rates. This consistent advantage under structural perturbations validates the enhanced robustness of our method, particularly in maintaining predictive stability when encountering incomplete graph information.

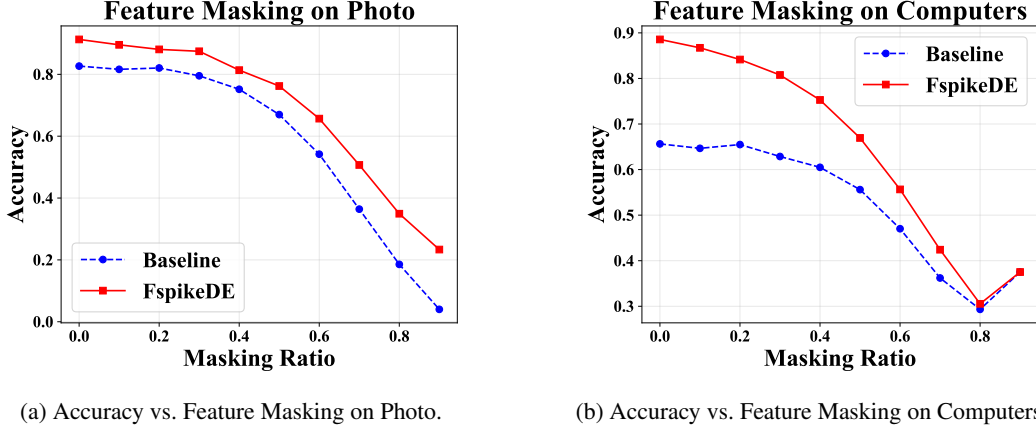


Figure 6: Robustness Comparison: Baseline vs. fspikeDE in Graph Learning under Feature Dropout Perturbations.

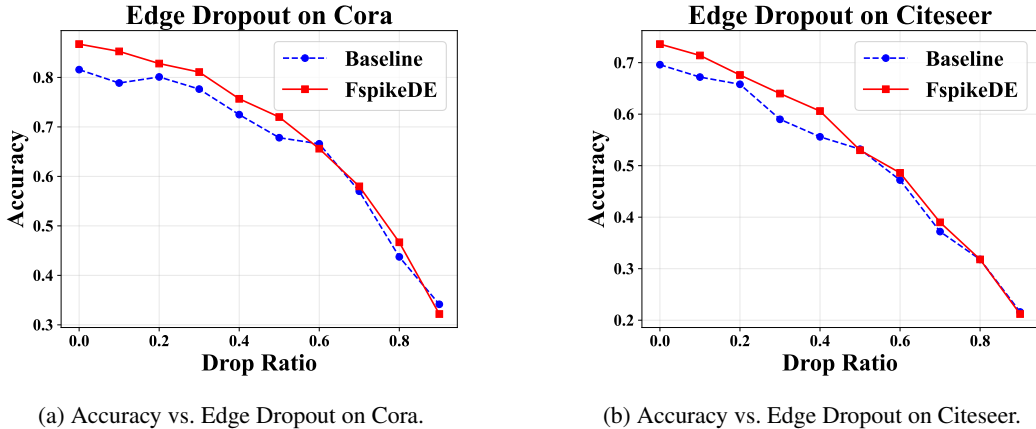


Figure 7: Structural Robustness Evaluation: Baseline vs. fspikeDE on Edge Dropout Scenarios in Citation Networks.

Image Classification Tasks.

Performance Under Different Data Sparsity Levels. To evaluate the performance of the network under varying levels of spike/event sparsity, we conducted experiments on both the MNIST and N-Caltech101 datasets. In our experiments, we applied different levels of data discard to the spike/event data. The results, as shown in Figure 8, demonstrate that our fspikeDE method consistently outperforms the SpikingJelly-based approach across all discard ratios. These results validate the superior robustness of our method under different levels of data sparsity.

Performance Under Different Levels of Spike Noise Interference. To evaluate the robustness of our method under various levels of spike noise interference, we added spike noise (with a value of 1) to the spike/event data at different ratios. As shown in Figure 9, our fspikeDE method demonstrates superior performance compared to the SpikingJelly-based approach across all spike noise ratios. These results validate the robustness of our method under varying levels of spike noise interference.

Robustness Under Different Levels of Object Occlusion. To test the irregular sampling scenarios with partially observed event series, we consider spike/event signal occlusion and introduce a zero-

value occlusion block at the center of the input signal. We investigated the impact of varying the size of the occlusion block on the experimental results. As shown in Figure 10, our fspikeDE method demonstrates stronger resistance to interference compared to the SpikingJelly-based approach across different occlusion block sizes. These results validate the robustness of our method under varying levels of object occlusion.

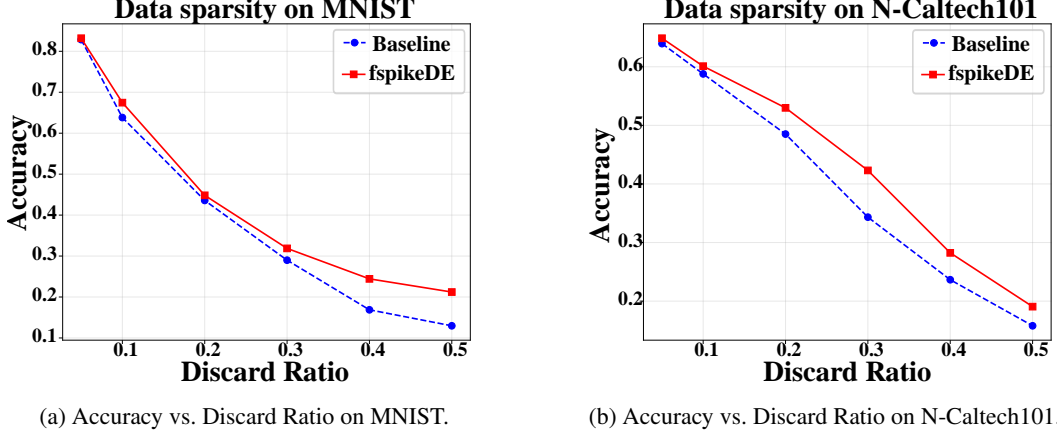


Figure 8: Robustness test on different discard ratios.

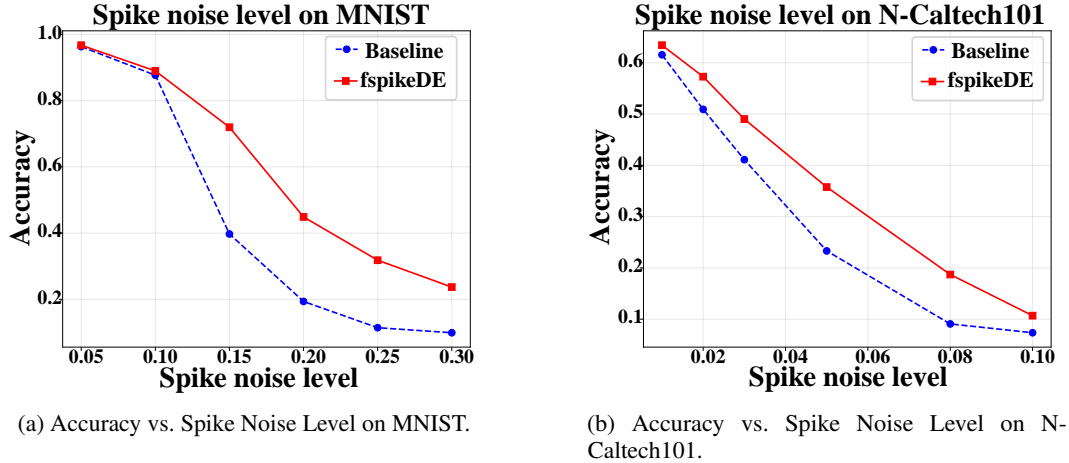


Figure 9: Robustness test on spike noise levels.

S4.3 Network structure and Energy Consumption

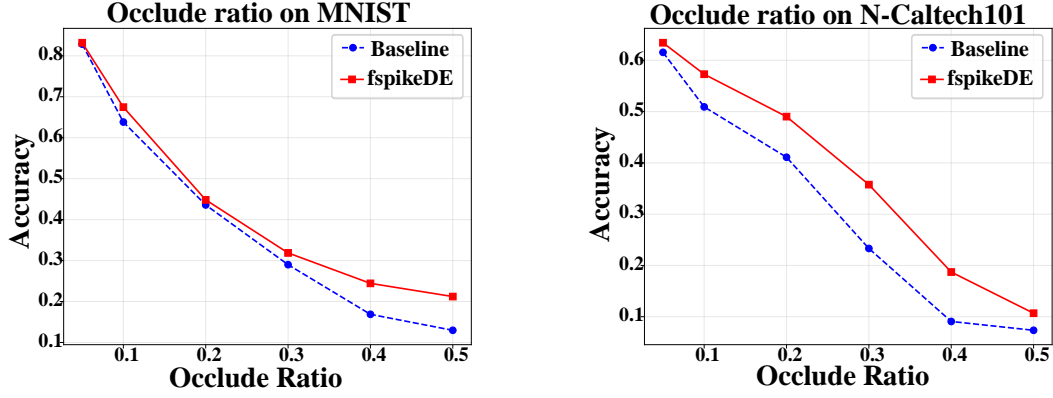
To intuitively demonstrate the energy consumption advantages of our proposed fspikeDE, we follow the methodology outlined in [9, 10] to calculate the energy consumption of the classification networks. The specific algorithm is as follows:

$$E_{MLP} = E_{AC} \cdot T \cdot R_M \cdot FL_{MLP}, \quad (45)$$

$$E_{Conv} = E_{MAC} \cdot T \cdot R_C \cdot FL_{Conv}, \quad (\text{first conv}) \quad (46)$$

$$E_{Conv} = E_{AC} \cdot T \cdot R_C \cdot FL_{Conv}. \quad (\text{other conv}) \quad (47)$$

Following [9, 10], we assume that the data for various operations are implemented using 32-bit floating-point arithmetic in 45nm technology, where $E_{MAC} = 4.6pJ$ and $E_{AC} = 0.9pJ$. Here, T represents the time steps, while R_M and R_C denote the average spiking firing rates of the neuron module. Additionally, FL_{MLP} and FL_{Conv} represent the FLOPs of the MLP and Conv layers, respectively.



(a) Accuracy vs. Occlude ratio on MNIST.

(b) Accuracy vs. Occlude ratio on N-Caltech101.

Figure 10: Robustness test on occlude ratios.

Based on this, we record the relevant network structures and the average spiking fire rate. The results are presented in Table 8, Table 9, Table 10 and Table 11. From the calculation results, it can be observed that our method achieves higher performance while maintaining lower energy consumption compared to the approach implemented with SpikingJelly.

Table 8: The architecture of the sequential spiking neural network on the MNIST dataset and its spiking firing rate are analyzed. Blue indicates the average spiking firing rate over T steps and overall energy using SpikingJelly, while Red represents using fspikeDE.

Layer Type	Details
Conv2d	Input: 1, Output: 64, kernel=3, stride=1, padding=1
LIFNeuron	0.0446 0.0248
Conv2d	Input: 64, Output: 64, kernel=3, stride=1, padding=1
LIFNeuron	0.0737 0.0240
Linear (MLP)	Input: 3136, Output: 256
LIFNeuron	0.3816 0.3084
Linear (MLP)	Input: 256, Output: 10
LIFNeuron	0.0996 0.0741
Energy	0.038mJ 0.015mJ

Table 9: The architecture of the sequential spiking neural network on the **Fashion-MNIST** dataset and its spiking firing rate are analyzed. **Blue** indicates the average spiking firing rate over T steps and overall energy using SpikingJelly, while **Red** represents using fspikeDE.

Layer Type	Details
Conv2d	Input: 1, Output: 64, kernel=3, stride=1, padding=1
LIFNeuron	0.0367 0.0505
Conv2d	Input: 64, Output: 64, kernel=3, stride=1, padding=1
LIFNeuron	0.0781 0.0266
Linear (MLP)	Input: 3136, Output: 256
LIFNeuron	0.3112 0.2939
Linear (MLP)	Input: 256, Output: 10
LIFNeuron	0.0987 0.0836
Energy	0.038mJ 0.018mJ

Table 10: The architecture of the sequential spiking neural network on the **DVSGesture128** dataset and its spiking firing rate are analyzed. **Blue** indicates the average spiking firing rate over T steps and overall energy using SpikingJelly, while **Red** represents using fspikeDE.

Layer Type	Details
Conv2d	Input: 2, Output: 128, kernel=3, stride=1, padding=1
LIFNeuron	0.0132 0.0355
Conv2d	Input: 128, Output: 128, kernel=3, stride=1, padding=1
LIFNeuron	0.0220 0.0202
Conv2d	Input: 128, Output: 128, kernel=3, stride=1, padding=1
LIFNeuron	0.0256 0.0240
Conv2d	Input: 128, Output: 128, kernel=3, stride=1, padding=1
LIFNeuron	0.0332 0.0128
Conv2d	Input: 128, Output: 128, kernel=3, stride=1, padding=1
LIFNeuron	0.0733 0.0522
Linear (MLP)	Input: 2048, Output: 512
LIFNeuron	0.3329 0.2602
Linear (MLP)	Input: 512, Output: 110
LIFNeuron	0.0895 0.0725
VotingLayer	–
Energy	5.38mJ 3.89mJ

Table 11: The architecture of the sequential spiking neural network on the **N-Caltech101** dataset and its spiking firing rate are analyzed. **Blue** indicates the average spiking firing rate over T steps and overall energy using SpikingJelly, while **Red** represents using fspikeDE.

Layer Type	Details
Conv2d	Input: 2, Output: 128, kernel=3, stride=1, padding=1
LIFNeuron	0.0134 0.0532
Conv2d	Input: 128, Output: 128, kernel=3, stride=1, padding=1
LIFNeuron	0.0435 0.0223
Conv2d	Input: 128, Output: 128, kernel=3, stride=1, padding=1
LIFNeuron	0.0497 0.0433
Conv2d	Input: 128, Output: 128, kernel=3, stride=1, padding=1
LIFNeuron	0.0647 0.0518
Conv2d	Input: 128, Output: 128, kernel=3, stride=1, padding=1
LIFNeuron	0.0949 0.1077
Linear (MLP)	Input: 2048, Output: 512
LIFNeuron	0.3684 0.3058
Linear (MLP)	Input: 512, Output: 101
LIFNeuron	0.0533 0.0395
VotingLayer	–
Energy	8.81mJ 7.96mJ

S5 Toolbox “fspikeDE” Presentation

We propose a novel toolbox, `fspikeDE`, built upon the PyTorch framework. This toolbox enables the construction of SNNs through interfaces highly similar to those in PyTorch. The directory structure of the toolbox is as follows:

```
.
├── __init__.py          # Package initialization
├── layer.py            # Base layer definitions
├── neuron.py          # Neuron model implementations
├── odefunc.py         # ODE function definitions for SNNs
├── snn.py             # High-level SNN construction interface
├── surrogate.py       # Surrogate gradient implementations
└── utils.py           # Utility functions
```

The `neuron` module provides three types of neurons: `LIFNeuron`, which represents the Leaky Integrate-and-Fire neuron model; `IFNeuron`, which corresponds to the Integrate-and-Fire neuron model; and `HardResetLIFNeuron`, a variant of the LIF neuron with a hard reset mechanism. These neuron types represent the commonly used models in SNNs.

The `snn` module offers a high-level interface for quickly constructing SNNs with two key functionalities. First, it supports the direct conversion of ANNs into SNNs. Second, it encapsulates SNNs into network objects that support both forward propagation with spike generation and backward propagation using surrogate gradients.

By using the `snn` module, constructing a spiking neural network becomes straightforward and efficient.

Usage instructions

Convert an artificial neural network into a spiking neural network:

```
from spikeDE import snn
import torch.nn as nn

# Define an artificial neural network (ANN)
ann = nn.Sequential(
    nn.Conv2d(in_channels=1, out_channels=32, kernel_size=3, padding=1),
    nn.Sigmoid(),
    nn.MaxPool2d(kernel_size=2),

    nn.Conv2d(in_channels=32, out_channels=64, kernel_size=3, padding=1),
    nn.Sigmoid(),
    nn.MaxPool2d(kernel_size=2),

    nn.Flatten(),
    nn.Linear(3136, 128),
    nn.Sigmoid(),
    nn.Linear(128, 10),
    nn.Softmax()
)

# Convert ANN to SNN with specified parameters
snn_model = snn(
    ann,
    input_type="ann",
    neuron_type="LIF",
    tau=2.0,
    threshold=1.0,
    surrogate_grad_scale=5.0,
    integrator="fdeint_adjoint",
    beta=0.8
```

)

Or you can directly build a spiking neural network using the neurons we provide:

```
from spikeDE import snn, LIFNeuron
import torch.nn as nn

# Build SNN directly with spiking neurons
snet = nn.Sequential(
    nn.Conv2d(in_channels=1, out_channels=32, kernel_size=3, padding=1),
    LIFNeuron(tau=2.0, threshold=1.0, surrogate_grad_scale=5),
    nn.MaxPool2d(kernel_size=2),

    nn.Conv2d(in_channels=32, out_channels=64, kernel_size=3, padding=1),
    LIFNeuron(tau=2.0, threshold=1.0, surrogate_grad_scale=5),
    nn.MaxPool2d(kernel_size=2),

    nn.Flatten(),
    nn.Linear(3136, 128),
    LIFNeuron(tau=2.0, threshold=1.0, surrogate_grad_scale=5),
    nn.Linear(128, 10),
    LIFNeuron(tau=2.0, threshold=1.0, surrogate_grad_scale=5),
)

# Wrap the network with SNN interface
snn_model = snn(snet,
                integrator="fdeint_adjoint",
                beta=0.8)
```

The resulting spiking neural network (SNN) model can be directly used for training. The model accepts an input $\mathbf{X} \in \mathbb{R}^{T \times N \times *}$, where T represents the length of the spike time steps and N denotes the batch size. The output of the model, denoted as \mathbf{O} , is a tuple that includes the membrane potential of each layer at each time step and the accumulated spikes of the last layer.

For the **integrator**, two options are available. The first option, `odeint_adjoint`, is an integer-order spiking differential equation integrator, which supports the solver `euler`. The second option, `fdeint_adjoint`, is a fractional-order spiking differential equation integrator. This integrator supports multiple FDE solvers, including `predictor-f`, `predictor-o`, `gl-f`, `gl-o`, `trap-f`, and `trap-o`. These integrators provide flexibility in modeling both integer-order and fractional-order dynamics in SNNs.

We take these two integrators as examples to build the forward and backward propagation frameworks for the network:

```
def train(args, model, device, train_loader, optimizer, criterion, epoch):
    """
    Train the model for one epoch

    Args:
        args: Training configuration parameters
        model: Spiking neural network model
        device: Computing device (CPU/GPU)
        train_loader: Data loader for training set
        optimizer: Optimizer for parameter updates
        criterion: Loss function
        epoch: Current training epoch
    """
    model.train()
    for batch_idx, (data, target) in enumerate(train_loader):
        # Data shape: [T, N, *], where T=time steps, N=batch size
        data, target = data.to(device), target.to(device)
```

```

# Generate time points for integration
# Spans from 0 to (T-1)*time_interval with T evenly spaced points
data_time = torch.linspace(
    0, args.time_interval * (args.T - 1), args.T, device=device
).float()

# Select integration method
method = "euler"
# Integration method selection:
# - For odeint_adjoint (integer-order): only support 'euler'
# - For fdeint_adjoint (fractional-order):
#   supports 'predictor-f', 'predictor-o', 'trap-f',
#   'trap-o', 'gl-f', 'gl-o' methods

# Set integration options (step size for numerical methods)
options = {'step_size': 0.01}

# Clear gradients before backward pass
optimizer.zero_grad()

# Generate output time points
# Can be adjusted to reduce memory usage (e.g., save intermediate steps)
output_time = torch.linspace(
    0, args.time_interval * (args.T - 1), args.T, device=device
).float()

# Output format: Tuple containing membrane potentials and spikes
output = model(data, data_time, output_time, method, options)

# output[-1][-1] corresponds to the final layer's spikes
loss = criterion(output[-1][-1], target)

loss.backward()
optimizer.step()
....

```

Specifically, for an `snn_model` containing n spiking neurons:

The first n elements in `output`, denoted as $O_i \in \mathbb{R}^{T \times N \times *}$ ($i = 1, 2, \dots, n$), represent the membrane potentials of each neuron at each time step. The last element, $O_{n+1} \in \mathbb{R}^{T \times N \times *}$, corresponds to the accumulated spikes of the final neuron over time. Thus, `output[-1][-1]` corresponds to the accumulated spikes of the last neuron at the final time step.

Users have the flexibility to decide how to use the `snn_model`'s output for their specific applications.

S6 Limitations and Broader Impacts

S6.1 Limitations

First, the hyperparameter tuning process for fractional dynamics, such as selecting the fractional order and decay parameters, can be non-trivial and requires domain expertise or extensive experimentation. This may pose challenges for practitioners aiming to deploy the framework in new applications. **Second**, while our experiments demonstrate robustness to noise and superior performance on several datasets, the method has not been extensively tested on ultra-large-scale datasets (e.g., ImageNet) or real-time systems where latency is critical. Further research is needed to evaluate the practical constraints of deploying `fspikeDE` in such environments.

S6.2 Broader Impacts

The proposed fspikeDE framework introduces a biologically inspired approach to spiking neural networks, with the potential for significant positive impact on both research and application domains. By incorporating fractional-order dynamics, fspikeDE advances the modeling of complex temporal dependencies, offering new insights into brain-like computation and contributing to the understanding of non-Markovian behavior in biological neurons. This could inspire further interdisciplinary research in neuroscience and machine learning.

From an application perspective, the ability of fspikeDE to process temporal information with enhanced accuracy and energy efficiency makes it well-suited for tasks such as edge computing, Internet of Things (IoT) devices, and neuromorphic hardware. The open-sourced toolbox provides a practical resource for researchers and practitioners, potentially accelerating innovation in fields like computational neuroscience, robotics, and bio-inspired artificial intelligence.

However, as with any machine learning framework, ethical considerations must be addressed. The deployment of fspikeDE in sensitive applications, such as autonomous systems or decision-making tasks, should be carefully evaluated to avoid unintended consequences. Additionally, the increased computational requirements of fractional dynamics raise concerns about energy consumption during training, which may counteract the energy efficiency benefits of SNNs in some scenarios. Responsible use, combined with efforts to improve computational efficiency, will be essential to maximize the positive societal impact of this technology.

References

- [1] S. Hochreiter and J. Schmidhuber, "Long short-term memory," *Neural computation*, vol. 9, no. 8, pp. 1735–1780, 1997.
- [2] A. Krizhevsky, I. Sutskever, and G. E. Hinton, "Imagenet classification with deep convolutional neural networks," *Advances in neural information processing systems*, vol. 25, 2012.
- [3] K. Simonyan and A. Zisserman, "Very deep convolutional networks for large-scale image recognition," *arXiv preprint arXiv:1409.1556*, 2014.
- [4] Y. LeCun, Y. Bengio, and G. Hinton, "Deep learning," *nature*, vol. 521, no. 7553, pp. 436–444, 2015.
- [5] A. Vaswani, N. Shazeer, N. Parmar, J. Uszkoreit, L. Jones, A. N. Gomez, Ł. Kaiser, and I. Polosukhin, "Attention is all you need," *Advances in neural information processing systems*, vol. 30, 2017.
- [6] A. Gu and T. Dao, "Mamba: Linear-time sequence modeling with selective state spaces," *arXiv preprint arXiv:2312.00752*, 2023.
- [7] P. Dhar, "The carbon impact of artificial intelligence," *Nature Machine Intelligence*, vol. 2, no. 8, pp. 423–425, Aug 2020.
- [8] G. Gallego, T. Delbrück, G. Orchard, C. Bartolozzi, B. Taba, A. Censi, S. Leutenegger, A. J. Davison, J. Conradt, K. Daniilidis *et al.*, "Event-based vision: A survey," *IEEE Trans. Pattern Anal. Mach. Intell.*, vol. 44, no. 1, pp. 154–180, 2020.
- [9] M. Yao, J. Hu, Z. Zhou, L. Yuan, Y. Tian, B. Xu, and G. Li, "Spike-driven transformer," *Advances in neural information processing systems*, vol. 36, pp. 64 043–64 058, 2023.
- [10] M. Yao, J. Hu, T. Hu, Y. Xu, Z. Zhou, Y. Tian, B. Xu, and G. Li, "Spike-driven transformer v2: Meta spiking neural network architecture inspiring the design of next-generation neuromorphic chips," *arXiv preprint arXiv:2404.03663*, 2024.
- [11] W. Li, H. Chen, J. Guo, Z. Zhang, and Y. Wang, "Brain-inspired multilayer perceptron with spiking neurons," in *CVPR*, 2022, pp. 783–793.
- [12] L. Zhu, X. Wang, Y. Chang, J. Li, T. Huang, and Y. Tian, "Event-based video reconstruction via potential-assisted spiking neural network," in *CVPR*, 2022, pp. 3594–3604.
- [13] Z. Wu, H. Zhang, Y. Lin, G. Li, M. Wang, and Y. Tang, "Liaf-net: Leaky integrate and analog fire network for lightweight and efficient spatiotemporal information processing," *IEEE Trans. Neural Netw. Learn. Syst.*, vol. 33, no. 11, pp. 6249–6262, 2021.

- [14] C. Ge, X. Fu, P. He, K. Wang, C. Cao, and Z.-J. Zha, “Neuromorphic event signal-driven network for video de-raining,” in *Proceedings of the AAAI Conference on Artificial Intelligence*, vol. 38, no. 3, 2024, pp. 1878–1886.
- [15] Y. Wang, M. Zhang, Y. Chen, and H. Qu, “Signed neuron with memory: Towards simple, accurate and high-efficient ann-snn conversion,” in *IJCAI*, 2022.
- [16] K. Roy, A. Jaiswal, and P. Panda, “Towards spike-based machine intelligence with neuromorphic computing,” *Nature*, vol. 575, no. 7784, pp. 607–617, 2019.
- [17] C. D. Schuman, S. R. Kulkarni, M. Parsa, J. P. Mitchell, P. Date, and B. Kay, “Opportunities for neuromorphic computing algorithms and applications,” *Nature Computational Science*, vol. 2, no. 1, pp. 10–19, 2022.
- [18] B. Yin, F. Corradi, and S. M. Bohté, “Accurate and efficient time-domain classification with adaptive spiking recurrent neural networks,” *Nature Machine Intelligence*, vol. 3, no. 10, pp. 905–913, 2021.
- [19] A. Rao, P. Plank, A. Wild, and W. Maass, “A long short-term memory for ai applications in spike-based neuromorphic hardware,” *Nature Machine Intelligence*, vol. 4, no. 5, pp. 467–479, 2022.
- [20] W. Fang, Z. Yu, Y. Chen, T. Huang, T. Masquelier, and Y. Tian, “Deep residual learning in spiking neural networks,” *Advances in Neural Information Processing Systems*, vol. 34, pp. 21 056–21 069, 2021.
- [21] H. Zheng, Y. Wu, L. Deng, Y. Hu, and G. Li, “Going deeper with directly-trained larger spiking neural networks,” in *Proceedings of the AAAI conference on artificial intelligence*, vol. 35, no. 12, 2021, pp. 11 062–11 070.
- [22] Y. Hu, L. Deng, Y. Wu, M. Yao, and G. Li, “Advancing spiking neural networks toward deep residual learning,” *IEEE transactions on neural networks and learning systems*, vol. 36, no. 2, pp. 2353–2367, 2024.
- [23] M. Yao, G. Zhao, H. Zhang, Y. Hu, L. Deng, Y. Tian, B. Xu, and G. Li, “Attention spiking neural networks,” *IEEE transactions on pattern analysis and machine intelligence*, vol. 45, no. 8, pp. 9393–9410, 2023.
- [24] X. Qiu, R.-J. Zhu, Y. Chou, Z. Wang, L.-j. Deng, and G. Li, “Gated attention coding for training high-performance and efficient spiking neural networks,” in *Proceedings of the AAAI Conference on Artificial Intelligence*, vol. 38, no. 1, 2024, pp. 601–610.
- [25] X. Luo, M. Yao, Y. Chou, B. Xu, and G. Li, “Integer-valued training and spike-driven inference spiking neural network for high-performance and energy-efficient object detection,” in *European Conference on Computer Vision*. Springer, 2024, pp. 253–272.
- [26] M. Yao, H. Zhang, G. Zhao, X. Zhang, D. Wang, G. Cao, and G. Li, “Sparsen spiking activity can be better: Feature refine-and-mask spiking neural network for event-based visual recognition,” *Neural Networks*, vol. 166, pp. 410–423, 2023.
- [27] M. Yao, H. Gao, G. Zhao, D. Wang, Y. Lin, Z. Yang, and G. Li, “Temporal-wise attention spiking neural networks for event streams classification,” in *Proceedings of the IEEE/CVF international conference on computer vision*, 2021, pp. 10 221–10 230.
- [28] E. Hunsberger and C. Eliasmith, “Spiking deep networks with lif neurons,” *arXiv preprint arXiv:1510.08829*, 2015.
- [29] A. L. Hodgkin and A. F. Huxley, “A quantitative description of membrane current and its application to conduction and excitation in nerve,” *The Journal of physiology*, vol. 117, no. 4, p. 500, 1952.
- [30] Y. Wu, L. Deng, G. Li, J. Zhu, and L. Shi, “Spatio-temporal backpropagation for training high-performance spiking neural networks,” *Frontiers in neuroscience*, vol. 12, p. 331, 2018.
- [31] J. K. Eshraghian, M. Ward, E. O. Neftci, X. Wang, G. Lenz, G. Dwivedi, M. Bennamoun, D. S. Jeong, and W. D. Lu, “Training spiking neural networks using lessons from deep learning,” *Proceedings of the IEEE*, vol. 111, no. 9, pp. 1016–1054, 2023.
- [32] N. Ulanovsky, L. Las, D. Farkas, and I. Nelken, “Multiple time scales of adaptation in auditory cortex neurons,” *Journal of Neuroscience*, vol. 24, no. 46, pp. 10 440–10 453, 2004.

- [33] G. La Camera, A. Rauch, D. Thurbon, H.-R. Luscher, W. Senn, and S. Fusi, “Multiple time scales of temporal response in pyramidal and fast spiking cortical neurons,” *Journal of neurophysiology*, vol. 96, no. 6, pp. 3448–3464, 2006.
- [34] K. D. Miller and T. W. Troyer, “Neural noise can explain expansive, power-law nonlinearities in neural response functions,” *Journal of neurophysiology*, vol. 87, no. 2, pp. 653–659, 2002.
- [35] W. Spain, P. Schwindt, and W. Crill, “Two transient potassium currents in layer v pyramidal neurones from cat sensorimotor cortex,” *The Journal of physiology*, vol. 434, no. 1, pp. 591–607, 1991.
- [36] G. Gilboa, R. Chen, and N. Brenner, “History-dependent multiple-time-scale dynamics in a single-neuron model,” *Journal of Neuroscience*, vol. 25, no. 28, pp. 6479–6489, 2005.
- [37] A. D. Coop, H. Cornelis, and F. Santamaria, “Dendritic excitability modulates dendritic information processing in a purkinje cell model,” *Frontiers in computational neuroscience*, vol. 4, p. 827, 2010.
- [38] C. Kirch and L. L. Gollo, “Spatially resolved dendritic integration: Towards a functional classification of neurons,” *PeerJ*, vol. 8, p. e10250, 2020.
- [39] K. Diethelm, *The analysis of fractional differential equations: an application-oriented exposition using differential operators of Caputo type*. Lect. Notes Math., 2010, vol. 2004.
- [40] D. Baleanu, K. Diethelm, E. Scalas, and J. J. Trujillo, *Fractional calculus: models and numerical methods*. World Scientific, 2012, vol. 3.
- [41] W. Teka, T. M. Marinov, and F. Santamaria, “Neuronal spike timing adaptation described with a fractional leaky integrate-and-fire model,” *PLoS computational biology*, vol. 10, no. 3, p. e1003526, 2014.
- [42] Y. Deng, B. Liu, Z. Huang, X. Liu, S. He, Q. Li, and D. Guo, “Fractional spiking neuron: Fractional leaky integrate-and-fire circuit described with dendritic fractal model,” *IEEE Transactions on Biomedical Circuits and Systems*, vol. 16, no. 6, pp. 1375–1386, 2022.
- [43] G. E. Ha and E. Cheong, “Spike frequency adaptation in neurons of the central nervous system,” *Experimental neurobiology*, vol. 26, no. 4, p. 179, 2017.
- [44] H. T. Lee and D. M. Monahan, “Exploring fractional leaky integrate-and-fire neurons in spiking neural networks,” *Artem Arefev*, p. 138.
- [45] W. Fang, Y. Chen, J. Ding, Z. Yu, T. Masquelier, D. Chen, L. Huang, H. Zhou, G. Li, and Y. Tian, “Spikingjelly: An open-source machine learning infrastructure platform for spike-based intelligence,” *Science Advances*, vol. 9, no. 40, p. eadi1480, 2023.
- [46] P. J. Werbos, “Backpropagation through time: what it does and how to do it,” *Proceedings of the IEEE*, vol. 78, no. 10, pp. 1550–1560, 1990.
- [47] Q. Kang, K. Zhao, Y. Song, Y. Xie, Y. Zhao, S. Wang, R. She, and W. P. Tay, “Coupling graph neural networks with fractional order continuous dynamics: A robustness study,” in *Proc. AAAI Conference on Artificial Intelligence*, Vancouver, Canada, Feb. 2024.
- [48] J. Sabatier, P. Lanusse, P. Melchior, and A. Oustaloup, “Fractional order differentiation and robust control design,” *Intelligent systems, control and automation: science and engineering*, vol. 77, pp. 13–18, 2015.
- [49] V. E. Tarasov, *Fractional dynamics: applications of fractional calculus to dynamics of particles, fields and media*. Springer Science & Business Media, 2011.
- [50] K. Diethelm, N. J. Ford, and A. D. Freed, “Detailed error analysis for a fractional adams method,” *Numer. Algorithms*, vol. 36, pp. 31–52, 2004.
- [51] Z. Zhu, J. Peng, J. Li, L. Chen, Q. Yu, and S. Luo, “Spiking graph convolutional networks,” *arXiv preprint arXiv:2205.02767*, 2022.
- [52] H. Zhao, X. Yang, C. Deng, and J. Yan, “Dynamic reactive spiking graph neural network,” in *Proceedings of the AAAI Conference on Artificial Intelligence*, vol. 38, no. 15, 2024, pp. 16970–16978.
- [53] L. Sun, Z. Huang, Q. Wan, H. Peng, and P. S. Yu, “Spiking graph neural network on riemannian manifolds,” *arXiv preprint arXiv:2410.17941*, 2024.

- [54] A. K. McCallum, K. Nigam, J. Rennie, and K. Seymore, "Automating the construction of internet portals with machine learning," *Information Retrieval*, vol. 3, pp. 127–163, 2000.
- [55] P. Sen, G. Namata, M. Bilgic, L. Getoor, B. Galligher, and T. Eliassi-Rad, "Collective classification in network data," *AI magazine*, vol. 29, no. 3, pp. 93–93, 2008.
- [56] X. Wang, H. Ji, C. Shi, B. Wang, Y. Ye, P. Cui, and P. S. Yu, "Heterogeneous graph attention network," in *The world wide web conference*, 2019, pp. 2022–2032.
- [57] W. Hu, M. Fey, M. Zitnik, Y. Dong, H. Ren, B. Liu, M. Catasta, and J. Leskovec, "Open graph benchmark: Datasets for machine learning on graphs," *arXiv:2005.00687*, 2020.
- [58] O. Shchur, M. Mumme, A. Bojchevski, and S. Günnemann, "Pitfalls of graph neural network evaluation," *Relational Representation Learn. Workshop, Advances Neural Inf. Process. Syst.*, 2018.
- [59] V. P. Dwivedi, C. K. Joshi, A. T. Luu, T. Laurent, Y. Bengio, and X. Bresson, "Benchmarking graph neural networks," *Journal of Machine Learning Research*, vol. 24, no. 43, pp. 1–48, 2023.
- [60] V. P. Dwivedi, A. T. Luu, T. Laurent, Y. Bengio, and X. Bresson, "Graph neural networks with learnable structural and positional representations," *arXiv preprint arXiv:2110.07875*, 2021.
- [61] M. J. Hall, "Gaussian noise and quantum-optical communication," *Physical Review A*, vol. 50, no. 4, p. 3295, 1994.
- [62] L. Deng, "The mnist database of handwritten digit images for machine learning research [best of the web]," *IEEE signal processing magazine*, vol. 29, no. 6, pp. 141–142, 2012.
- [63] H. Xiao, K. Rasul, and R. Vollgraf, "Fashion-mnist: a novel image dataset for benchmarking machine learning algorithms," *arXiv preprint arXiv:1708.07747*, 2017.
- [64] A. Amir, B. Taba, D. Berg, T. Melano, J. McKinstry, C. Di Nolfo, T. Nayak, A. Andreopoulos, G. Garreau, M. Mendoza *et al.*, "A low power, fully event-based gesture recognition system," in *Proceedings of the IEEE conference on computer vision and pattern recognition*, 2017, pp. 7243–7252.
- [65] G. Orchard, A. Jayawant, G. K. Cohen, and N. Thakor, "Converting static image datasets to spiking neuromorphic datasets using saccades," *Frontiers in neuroscience*, vol. 9, p. 437, 2015.
- [66] L. F. Abbott, "Lapicque's introduction of the integrate-and-fire model neuron (1907)," *Brain research bulletin*, vol. 50, no. 5-6, pp. 303–304, 1999.
- [67] R. Brette and W. Gerstner, "Adaptive exponential integrate-and-fire model as an effective description of neuronal activity," *Journal of neurophysiology*, vol. 94, no. 5, pp. 3637–3642, 2005.
- [68] A. Tavanaei, M. Ghodrati, S. R. Kheradpisheh, T. Masquelier, and A. Maida, "Deep learning in spiking neural networks," *Neural networks*, vol. 111, pp. 47–63, 2019.
- [69] F. Mainardi, *Fractional calculus and waves in linear viscoelasticity: an introduction to mathematical models*. World Scientific, 2022.
- [70] I. Podlubny, "An introduction to fractional derivatives, fractional differential equations, to methods of their solution and some of their applications," *Math. Sci. Eng.*, vol. 198, no. 340, pp. 0924–34 008, 1999.
- [71] T. J. Anastasio, "The fractional-order dynamics of brainstem vestibulo-oculomotor neurons," *Biological cybernetics*, vol. 72, no. 1, pp. 69–79, 1994.
- [72] E. Kaslik and S. Sivasundaram, "Nonlinear dynamics and chaos in fractional-order neural networks," *Neural networks*, vol. 32, pp. 245–256, 2012.
- [73] R. Rakkiyappan, K. Udhayakumar, G. Velmurugan, J. Cao, and A. Alsaedi, "Stability and hopf bifurcation analysis of fractional-order complex-valued neural networks with time delays," *Advances in Difference Equations*, vol. 2017, pp. 1–25, 2017.
- [74] Y. Yang, Y. He, Y. Wang, and M. Wu, "Stability analysis of fractional-order neural networks: an lmi approach," *Neurocomputing*, vol. 285, pp. 82–93, 2018.
- [75] C. Xu, M. Liao, P. Li, Y. Guo, Q. Xiao, and S. Yuan, "Influence of multiple time delays on bifurcation of fractional-order neural networks," *Applied Mathematics and Computation*, vol. 361, pp. 565–582, 2019.

- [76] Q. Kang, K. Zhao, Q. Ding, F. Ji, X. Li, W. Liang, Y. Song, and W. P. Tay, “Unleashing the potential of fractional calculus in graph neural networks with FROND,” in *Proc. International Conference on Learning Representations*, 2024.
- [77] Q. Kang, K. Zhao, Y. Song, Y. Xie, Y. Zhao, S. Wang, R. She, and W. P. Tay, “Coupling graph neural networks with fractional order continuous dynamics: A robustness study,” in *Proc. AAAI Conference on Artificial Intelligence*, Vancouver, Canada, Feb. 2024.
- [78] N. M. Gyöngyössi, G. Eros, and J. Botzheim, “Exploring the effects of caputo fractional derivative in spiking neural network training,” *Electronics*, vol. 11, no. 14, p. 2114, 2022.
- [79] Y. Yang, R. M. Voyles, H. H. Zhang, and R. A. Nawrocki, “Fractional-order spike-timing-dependent gradient descent for multi-layer spiking neural networks,” *Neurocomputing*, vol. 611, p. 128662, 2025.
- [80] R. T. Chen, Y. Rubanova, J. Bettencourt, and D. Duvenaud, “Neural ordinary differential equations,” *arXiv preprint arXiv:1806.07366*, 2018.
- [81] E. Weinan, “A proposal on machine learning via dynamical systems,” *Communications in Mathematics and Statistics*, vol. 5, no. 1, pp. 1–11, 2017.
- [82] Y. Rubanova, R. T. Chen, and D. K. Duvenaud, “Latent ordinary differential equations for irregularly-sampled time series,” *Advances in neural information processing systems*, vol. 32, 2019.
- [83] P. Kidger, J. Morrill, J. Foster, and T. Lyons, “Neural controlled differential equations for irregular time series,” *Advances in neural information processing systems*, vol. 33, pp. 6696–6707, 2020.
- [84] Q. Kang, X. Li, K. Zhao, W. Cui, Y. Zhao, W. Deng, and W. P. Tay, “Efficient training of neural fractional-order differential equation via adjoint backpropagation,” in *Proc. AAAI Conference on Artificial Intelligence*, Philadelphia, USA, Feb. 2025.
- [85] T. C. Wunderlich and C. Pehle, “Event-based backpropagation can compute exact gradients for spiking neural networks,” *Scientific Reports*, vol. 11, no. 1, p. 12829, 2021.
- [86] H. Rebecq, R. Ranftl, V. Koltun, and D. Scaramuzza, “Events-to-video: Bringing modern computer vision to event cameras,” in *CVPR*, 2019, pp. 3857–3866.
- [87] E. O. Neftci, H. Mostafa, and F. Zenke, “Surrogate gradient learning in spiking neural networks: Bringing the power of gradient-based optimization to spiking neural networks,” *IEEE Signal Processing Magazine*, vol. 36, no. 6, pp. 51–63, 2019.
- [88] N. Xu, L. Wang, Z. Yao, and T. Okatani, “Mets: Motion-encoded time-surface for event-based high-speed pose tracking,” *International Journal of Computer Vision*, pp. 1–19, 2025.
- [89] C. Yu, Z. Gu, D. Li, G. Wang, A. Wang, and E. Li, “Stsc-snn: Spatio-temporal synaptic connection with temporal convolution and attention for spiking neural networks,” *Frontiers in Neuroscience*, vol. 16, p. 1079357, 2022.
- [90] J. Cuadrado, U. Raçon, B. R. Cottureau, F. Barranco, and T. Masquelier, “Optical flow estimation from event-based cameras and spiking neural networks,” *Frontiers in Neuroscience*, vol. 17, p. 1160034, 2023.
- [91] M. Isik, K. Tiwari, M. B. Eryilmaz, and I. C. Dikmen, “Accelerating sensor fusion in neuromorphic computing: A case study on loihi-2,” in *2024 IEEE High Performance Extreme Computing Conference (HPEC)*. IEEE, 2024, pp. 1–7.
- [92] M. Mathieu, M. Henaff, and Y. LeCun, “Fast training of convolutional networks through ffts,” *arXiv preprint arXiv:1312.5851*, 2013.
- [93] A. Griewank, “A mathematical view of automatic differentiation,” *Acta Numerica*, vol. 12, pp. 321–398, 2003.
- [94] W. Deng, “Short memory principle and a predictor–corrector approach for fractional differential equations,” *J. Comput. Appl. Math.*, vol. 206, no. 1, pp. 174–188, 2007.
- [95] I. Podlubny, *Fractional Differential Equations*. Academic Press, 1999.